Ultrasmall Liquid Droplets on Solid Surfaces: Production, Imaging, and Relevance for Current Wetting Research

Antonio Méndez-Vilas, Ana Belén Jódar-Reyes, and María Luisa González-Martín**

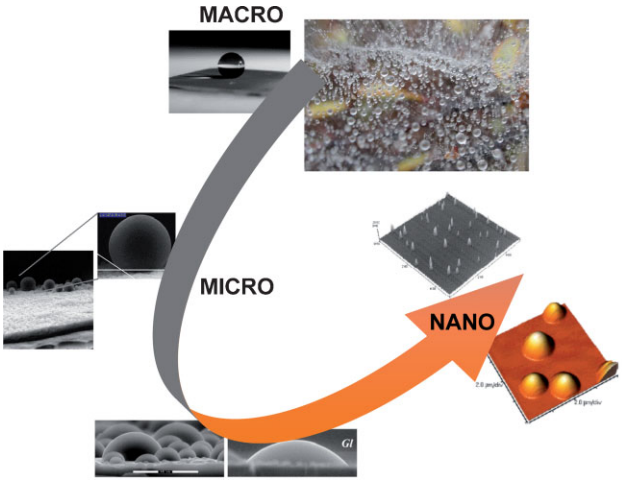

From the Contents

1. Justification, Theoretical Framework, and Experimental Techniques 1367
2. Discussion 1379
3. Summary and Outlook 1387

The investigation of micro- and nanoscale droplets on solid surfaces offers a wide range of research opportunities both at a fundamental and an applied level. On the fundamental side, advances in the techniques for production and imaging of such ultrasmall droplets will allow wetting theories to be tested down to the nanometer scale, where they predict the significant influence of phenomena such as the contact line tension or evaporation, which can be neglected in the case of macroscopic droplets. On the applied side, these advances will pave the way for characterizing a diverse set of industrially important materials such as textile or biomedical micro- and nanofibers, powdered solids, and topographically or chemically nanopatterned surfaces, as well as micro-and nanoscale devices, with relevance in diverse industries from biomedical to petroleum engineering. Here, the basic principles of wetting at the micro- and nanoscales are presented, and the essential characteristics of the main experimental techniques available for producing and imaging these droplets are described. In addition, the main fundamental and applied results are reviewed. The most problematic aspects of studying such ultrasmall droplets, and the developments that are in progress that are thought to circumvent them in the coming years, are highlighted.

Frontispiece image, from the top, anticlockwise: image courtesy of Dr. Luis Labajos-Brancano. Reproduced with permission from Reference [120], copyright 2003, American Chemical Society. Reproduced with permission from Reference [134], copyright 2005, Elsevier. Reproduced with permission from Reference [95], copyright 2001, Royal Microscopical Society. Reproduced with permission from Reference [52], copyright 2006, American Chemical Society. Reproduced with permission from Reference [29], copyright 2002, Elsevier.

NANO MICRO small

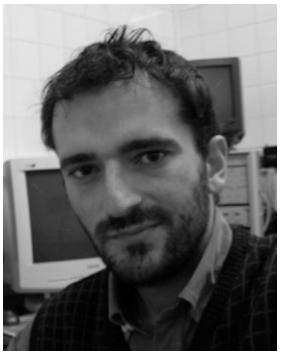

Antonio Méndez Vilas is currently a member of the AM-UEX research group of the CIBER-BBN Networking Research Center on Bioengineering, Biomaterials and Nanomedicine and the Biosurfaces & Interfacial Phenomena Group of the Department of Applied Physics of the University of Extremadura (UEX, Spain). He is also the Director of Formatex Research Center in Badajoz (Spain), with responsibilities over the management of R&D projects and organization of scientific events. His research interests cover the microscopic description of surfaces and interfacial phenomena, and as such he is interested in topics such as the wetting of solid surfaces, micro-/nanotopography and chemical heterogeneity of biotic (mainly micro-organisms) and abiotic (mainly biomaterials) surfaces, and initial microbial adhesion or biofilm formation.

Ana Belén Jódar Reyes is currently a Doctorate Lecturer in the Department of Applied Physics of the University of Extremadura (UEX, Spain). She is a member of the AM-UEX research group of the CIBER-BBN Networking Research Center on Bioengineering, Biomaterials and Nanomedicine and the Biosurfaces & Interfacial Phenomena Group of the UEX, and also of the Biocolloids and Fluid Physics Group of the University of Granada (UGR, Spain). Her scientific interests cover several aspects of the physics of interfaces, colloid systems, and complex fluids: colloidal stability, electrokinetics, adsorption of proteins, polymers and surfactants at interfaces, characterization of biomaterials at the macroscopic and nanoscopic level, and modeling of self-assembly of surfactants in solution and at interfaces.

María Luisa González Martín is the leader of the AM-UEX research group of the CIBER-BBN Networking Research Center on Bioengineering, Biomaterials and Nanomedicine and the Biosurfaces & Interfacial Phenomena Group of the Department of Applied Physics of the University of Extremadura (UEX, Spain). She has been involved in the organization of divulgative activities on Physics, and from 2004 to 2007 she took over the responsibility of Head of the UEX Department of Applied Physics. Her current interests cover several fundamental and applied topics, which include the wettability of extended and porous materials, relationships between macroscopic and microscopic characterization methods of solid surfaces, surface analysis and modification of biomaterials, and the interaction between biomaterials and micro-organisms, human cells and biomacromolecules.

1. Justification, Theoretical Framework, and Experimental Techniques

A note about terminology: in the literature, there is a certain ambiguity in relation to the terms ''microdroplet'' and ''nanodroplet,'' which in some cases might cause confusion. Some authors use the micro- or nano- prefix in the current micro- or nanotechnology context, in which the typical dimensions of the system are micro- or nanometers. However, many others use these prefixes to refer to micro- and nanoliter droplets. In this work, the first option will be followed. However, as we will sometimes refer to droplet volumes, it is convenient here to present a scheme to associate such small volumes with a certain dimensional scale (Figure 1).[1] For this, we will start with a cube of an edge length of 1 mm, which corresponds to a volume of 1 μL, and will subsequently divide the length of the cube by a factor of 10. In this review, we will specially address droplets in the picoliter to attoliter range.

1.1. Wetting and Contact Angle

Wettability is one of the basic features of solid surfaces. It can be defined as the tendency for a liquid to spread on a solid substrate. The laws of thermodynamics predict an equilibrium contact angle of a liquid droplet on a solid surface (that is, the degree of wetting) that is dependent on the interfacial Gibbs energies involved in the system. This contact angle is used for quantifying the wettability and related properties such as the solid surface Gibbs energy,[2–4] which are known to play a prime role in a variety of fundamental and technological processes.[5–9] The equilibrium contact angle of a non-reactive liquid on a solid is that which balances the interfacial energies, and it is termed the Young's contact angle (Equation 1). The solid is assumed to be smooth, homogeneous, rigid, and insoluble in the probe liquid. If the solid is rough but homogeneous, then the apparent contact angle is termed the Wenzel's angle, whereas for smooth and heterogeneous solids it is named the Cassie's angle. The above angles are static contact angles that are defined once the droplet spreading ceases. This is in contrast to dynamic contact angles, which are measured when the interface is moving; in the case of the interface moving towards the vapor, it is called the advancing contact angle, and in the case of moving away from the vapor, it is called the receding contact angle. As equilibrium contact

[*] A. Méndez-Vilas, Dr. M. L. González-Martín
Department of Applied Physics, University of Extremadura
Avda. Elvas s/n, 06071 Badajoz (Spain)
E-mail: amvilas@formatex.org; mlglez@unex.es

A. Méndez-Vilas, Dr. A. B. Jódar-Reyes, Dr. M. L. González-Martín
CIBER-BBN
Networked Biomedical Research Center in
Bioengineering, Biomaterials and Nanomedicine,
Badajoz (Spain)

Dr. A. B. Jódar-Reyes
Department of Applied Physics, University of Extremadura
Avda. Universidad s/n
10071, Cáceres (Spain)

DOI: 10.1002/smll.200800819

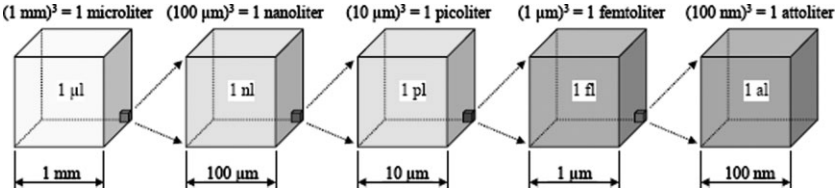

Figure 1. Schematic drawing to help associate a chosen volume with a dimensional scale. Reproduced with permission from Reference [1]. Copyright 2005, A. Meister.

angles are rarely achieved in practice, measured values have to be considered quasi-equilibrium contact angles.[5]

The most frequently used technique for measurement of the contact angles consists of settling a droplet of known volume on the solid surface, allowing it to spread until an equilibrium is reached, and analyzing the profile to extract the angle formed at the three-phase interface. This procedure is generally known as the sessile drop technique. It is assumed that the droplet is axisymmetric, at rest, and that its shape is dominated by interfacial tensions.[10]

The main equation used to quantify wetting phenomena is Young's equation

$$\cos\theta_{\text{Young}} = (\gamma_{\text{sv}} - \gamma_{\text{sl}})/\gamma_{\text{lv}} \tag{1}$$

where θ is the contact angle of the droplet and γ_{lv}, γ_{sl}, and γ_{sv} are the interfacial tensions between liquid/vapor, solid/liquid, and solid/vapor, respectively. Assuming a spherical cap-shape of the droplet (radius R, base radius r, maximum height H, and position of the droplet center x_c; Figure 2), which is expected for a liquid droplet resting on a surface assuming negligible influence of gravity, the contact angle of the droplet can be extracted as $\theta = 2\tan^{-1}(H/R)$. The equation of the circular line profile $z(x)$, which will be used later, can be expressed in terms of θ, r, and the position of the droplet center as

$$z(x) = \sqrt{\frac{r^2}{\sin^2\theta} - (x - x_c)^2} - r\cot\theta \tag{2}$$

Dupré defined the work of adhesion between solid and liquid as

$$W_{\text{sl}} = \gamma_{\text{sv}} + \gamma_{\text{lv}} + \gamma_{\text{sl}} \tag{3}$$

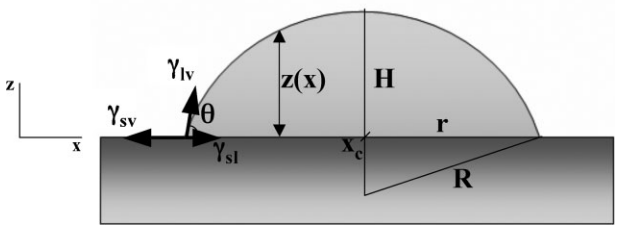

Figure 2. Equilibrium profile of a sessile droplet, with indication of the interfacial tensions acting at the three-phase line.

Insertion of this equation into Young's equation (Equation 1) yields the Young–Dupré equation:

$$W_{\text{sl}} = \gamma_{\text{lv}}(1 + \cos\theta) \tag{4}$$

For a given value of γ_{lv}, the contact angle increases as the adhesion between the liquid and solid decreases.

Even though Young's equation is extensively applied, it has been the focus of controversial scientific discussion because of its theoretical derivation as well as the fact that it is virtually impossible to prove experimentally. There are different limitations for the applicability of Young's equation. Several reports establish that this equation is macroscopic, and does not concern itself with the liquid surface in close vicinity of the contact line. Surface forces between the solid and the liquid surfaces modify the shape of the liquid surface on the nanoscopic scale. As a result, the nanoscopic contact angle might be different from the optically observable macroscopic contact angle. This effect is restricted to a drop thickness of typically 1–20 nm on top of the solid. In the case of small drops, it has been found that a new term related to a contact line tension (CLT) has to be added to Young's equation. An additional limitation is that due to the curved liquid surface, as its vapor pressure is always larger than that of its vapor, evaporation is unavoidable. While this effect is negligible in the case of macroscopic droplets, it might have an outstanding role when analyzing the shape of very small droplets.[11] Increasingly important technological developments in areas such as microfluidics and lab-on-chip systems require a precise knowledge of these effects involving ultrasmall amounts of liquids in contact with solids.

1.1.1. The Contact Line Tension

While a lot of experiments have shown an important variation of the contact angle as the drop sizes falls down to the micrometer-range, it is not clear whether this is a real phenomenon or an experimental artifact produced by the resolution of the imaging technique, especially because that the effect was mainly observed by using interferometry, when wavelengths are comparable to the size of the droplets.[12] Recently, atomic force microscopy (AFM), which has an imaging resolution in the nanometer range, has been used to explore the change of the wettability at small scales.[13]

The analysis of the size dependence of the contact angle has been traditionally addressed by introducing a phenomenological CLT, κ, acting at the three-phase contact line. By taking into account this line tension, the free energy minimization of a sessile drop yields the equation[14,15]

$$\gamma_{\text{sl}} - \gamma_{\text{sv}} + \gamma_{\text{lv}}\cos\theta + \frac{\kappa}{R\sin\theta} = 0 \tag{5}$$

where again R is the curvature radius of the drop assumed to be shaped as a spherical cap (the base radius, or the contact line radius, is $r = R\ \sin\ \theta$). Combining Equation 5 with Equation 1, the correction factor to be applied to the Young's

NANO MICRO small

contact angle due to the CLT is obtained as

$$\cos\theta = \cos\theta_{\text{Young}} - \frac{\kappa}{r\gamma_{\text{lv}}} \quad (6)$$

Both the local curvature and the contact angle can be obtained directly from a microscopy image of the liquid droplet resting on the solid substrate. The former can be obtained by fitting a specific portion of the contact line to a circle, and the latter can be obtained from a height profile taken across a line perpendicular to the portion of the contact line where the local curvature has been computed.

From an energetic point of view, the CLT can be defined as the excess free energy of a solid/liquid/vapor system per unit length of the three-phase contact line,[16] while from a mechanical point of view it can be seen as the linear tension due to the imbalance of the forces between molecules existing in and around the zone at which the three phases meet.[17] This line energy/tension is proportional to the drop perimeter and then scales as κr, while the surface energy/tension scales as $\gamma_{\text{lv}} r^2$. Thus, deviations of the contact angle from the macroscopic value are expected for a small droplet radius. Since the surface tension γ_{lv} is a typical intermolecular potential V divided by the square of a molecular size a, yielding some tens of mN m^{-1} for a generic liquid or solid only interacting through van der Waals forces, a CLT, κ, should be of the order of V/a, thus yielding about 10^{-11} N or J m^{-1} for similar systems.[18] A characteristic length scale for the influence of this tension can be estimated by dividing a typical CLT value by a typical surface tension value, that is, 10^{-11} J m^{-1}/10^{-2} J m^{-2} = 1 nm.[16] For extremely low values of the CLT it would be of practical importance only at the molecular-scale level, while for much larger values it might play a role in the performance of technological systems such as microfluidic devices.[17] The sign of the CLT depends on the nature of the different phases around the line.[18] For $\kappa < 0$, small droplets will better wet the solid (smaller contact angle, see Equation 6) than the larger ones, whereas the opposite will occur for $\kappa > 0$.

A second approach, called the interface displacement model, can be used for obtaining the CLT from a profile of a single droplet, and specifically from the deviation from the spherical cap shape in the vicinity of the three-phase line (currently only available with AFM). A redistribution of the liquid at the edge of the droplet takes place under the influence of an effective interface potential V(z). Thus, the mechanical equilibrium is reached, or, equivalently, its free energy is minimized. The CLT κ can be calculated from the effective interface potential $V(z)$ and the equilibrium profile $z(x,y)$.[19,20]

1.1.2. Evaporation of Ultrasmall Droplets

When droplets are created by direct deposition onto a surface (in contrast with nucleated droplets created from the vapor phase), care must be taken when interpreting their images as droplets might undergo some degree of evaporation before the images are collected. This is especially a problem when working with AFM as usually about 15–30 min are required for optimizing imaging parameters and acquiring the first images. Butt et al.[11] have shown that, assuming constant contact angle and temperature, a droplet with volume V_{L0} resting on a surface in saturated water vapor ambient conditions evaporates with a constant contact angle θ in time τ given by

$$\tau = \frac{1}{2\pi}\frac{V_{\text{LO}}}{D_{\text{f}}}\frac{k_{\text{B}}T}{P_0 V_{\text{m}}\lambda f} \quad (7)$$

where $f = 0.5(0.00008957 + 0.6333\theta + 0.116\theta^2 - 0.08878\theta^3 + 0.01033\theta^4)$ for $10^\circ \le \theta \le 180^\circ$, θ is expressed in radians, V_{m} is the molecular volume, P_0 is the vapor pressure, λ is the Kelvin's characteristic length, D_{f} is the diffusion constant of vapor molecules in the gas phase, T is the temperature, and k_{B} is the Boltzmann constant. For example, they showed that assuming a contact angle of 60°, $T = 25\,^\circ$C, a vapor pressure for water of 3169 Pa, $D_{\text{f}} = 5.3 \times 10^{-4}$ m^2 s^{-1}, and $\lambda = 1.04$ nm, a sessile droplet with a volume of 10 μm^3 (a reasonable volume for a small droplet produced by an atomizer) evaporates in 741 s. This is a time far lower than that required for acquiring stable AFM images of the liquid droplets. If saturation is not perfect and a value of "only" 99% relative humidity (RH) is reached, the evaporation time drastically drops to 10 s, making the situation even worse for the imaging of the droplets.

During evaporation, the droplet profile may vary in different ways. This was studied early in 1977 by Picknett and Bexon,[21] who concluded that a first "constant contact area" phase dominates until the contact angle decreases to a certain value, at which point the second "constant contact angle" phase dominates. This argument has been supported by other recent works, where evaporation of water microdroplets has been shown to progress from pinning (a decrease in contact angle accompanied by constant contact area) to shrinking (constant contact angle and a decrease in contact area).[22,23] Therefore, care must be taken when interpreting scale-dependent droplet profiles if evaporation might have occurred to some extent, as when experiments are undertaken under ambient conditions.

1.2. Generation of Ultrasmall Droplets on Solid Surfaces

The formation of stable microscopic and submicroscopic droplets on solid surfaces for wetting studies is not a trivial task. In order to atomize bulk liquid into droplets, energy has to be brought into the system. Mechanical energy can be added to the liquid by applying high pressure, vibration, or kinetic acceleration. Further, electric energy can be added to the system by applying a high voltage that separates the liquid body into droplets. Even heating the liquid to its boiling point can produce droplets. Air bubbles bursting at the liquid surface lead to the formation of droplets.[24] Different methods are available and they are reviewed in this section, especially those that have been applied to wetting studies.

In analogy with what is commonly done macroscopically in contact angle goniometry, we will first analyze the possibility of obtaining a micro- or nanoscale droplet deposited onto a substrate by its own weight from a capillary. Let us assume a

droplet of radius R_d of a liquid of density ρ_l and surface tension γ_{lv} hanging on a capillary of radius R_c. If gravity is the only force, F_g, to be used to overcome the surface tension forces, then the critical droplet size can be calculated by balancing the droplet weight

$$F_g = \frac{4}{3}\pi R_d^3 \rho_l g \quad (8)$$

and the force due to the surface tension, γ_{lv}

$$F_\gamma = 2\pi R_c \gamma_{lv} \quad (9)$$

The droplet will fall from the capillary when its radius overcomes a critical value of

$$R_{cr} = \left(\frac{3}{2}\frac{R_c \gamma_{lv}}{\rho_l g}\right)^{1/3} \quad (10)$$

For example, using a very thin capillary with a radius of 1 μm, a water droplet critical radius of 200 μm is obtained (200 times the capillary radius value). Therefore, it is readily seen that gravity alone cannot be used effectively to deposit microscopic or submicroscopic droplets on surfaces.

1.2.1. Spraying

The use of air sprayers and atomizers has been extensively explored with the aim of depositing small droplets onto solid surfaces to be further investigated by several imaging techniques. Small droplets are formed by mixing a liquid flowing with a chosen flow rate with pressurized air. The kinetic energy is used to overcome surface tension forces. The fine liquid jets break up into droplets. Spraying ultrafine drops is currently available from commercial atomizers, which allow one to produce droplets in a wide range of sizes, usually from a few to tens of micrometers. Liquids with viscosities up to about 1000 cP can be used.

Attempts have been made to deposit micro- and nanodroplets of liquids of different nature onto different kinds of surfaces. For example, Wang and coworkers used AFM to image droplets as small as tens of nanometers in diameter and a few nanometers height on the surface of previously sprayed surfaces like mica, Cu, Cr, Ni, Fe, and SUS304 steel under ambient conditions (Figure 3).[25–30] Evaporation effects were not discussed. They confirmed the liquid nature of those structures by observing their disappearance under scanning in contact mode. Pompe et al.[31] used this method to study the wetting behavior of diethylene glycol (DEG) droplets formed with an atomizer on Si wafers. The authors reported liquid drops of about 5–6 μm in size. They pointed out the disadvantage of using this liquid due to its evaporation, but they had time enough for imaging. Mugele et al.[32] also used standard vaporizers to deposit droplets of hexaethylene glycol (HEG) (chosen because of its low volatility and high surface tension) and reported droplet diameters between 0.1 and 25 μm under ambient conditions. A number of nonvolatile liquids such as glycerine, pentadecane, hexadecane, heptadecane, and others were also sprayed on

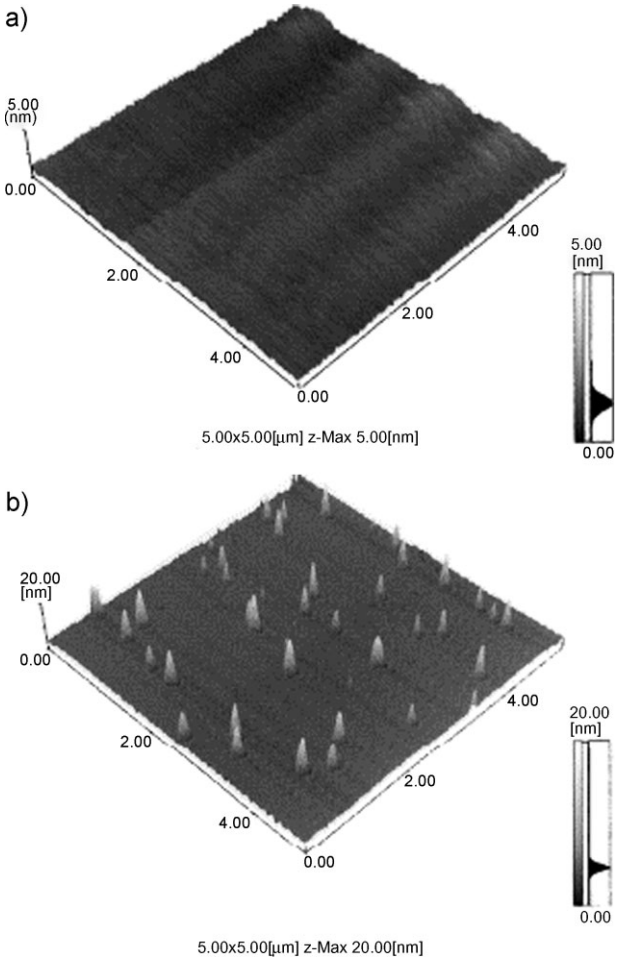

Figure 3. AFM images of a mica surface before (a) and after (b) water spraying. Reproduced with permission from Reference [29]. Copyright 2002, Elsevier Science.

several substrates (mica, glass, and Si wafers) and a large number of nano- and microdroplets were imaged using AFM. Evaporation could eventually be tracked in situ using AFM.

1.2.2. Electrospray

Electrostatic forces are used to create new droplets. This is based on the fact that liquids can readily interact with electric fields. Early in 1812, Lord Rayleigh reported that a liquid portraying an excessive charge (q) would disintegrate itself once the repulsive force between the charges overcomes the surface tension. A ''fissility'' factor X is used to describe the ratio of the electrical repulsive force to the surface force γ_{lv}

$$X = \frac{q^2}{64\pi^2 \gamma_{lv} \varepsilon_0 R^3} \leq 1 \quad (11)$$

where ε_0 is the dielectric constant of vacuum. A drop of $X \leq 1$ remains spherical, while for $X \approx 1$ it changes its shape by experiencing an elongation. For $X \gg 1$, the liquid is thrown in fine jets. A minireview on this issue has been recently published.[33] Submicroscopic droplets have been achieved

using electrospraying. To the authors' knowledge, only Jayasinghe and Edirisinghe[34] have used this method with a further characterization of the contact angles of the produced microdroplets. They used water, glycerine, and mixtures of both and assumed a negligible evaporation effect. In a typical electrospray setup, a liquid stream is forced through a needle at a potential difference of thousands of volts between it and a plate, thus accelerating formed droplets towards the counter-electrode. During their flight, they lose some mass by evaporation, which increases the surface charge and then the coulombic repulsion, and reduces even further the droplet size. As a consequence, a cloud of charged liquid droplets whose size can be made quite small (less than 1 μm) is obtained.[35–38] A drawback is that size disparity tends to be highly sensitive to experimental parameters.[39] However, this could be a positive point if droplets of different sizes are desired to study scale-dependent wetting properties. Recently, Paine et al.[40] have reported a controlled electrospray-pulsation method for deposition of femtoliter fluid droplets onto surfaces. Adhikari and Fernando[41] have also presented a method to produce glycerine nanodroplets (mean dimension ≈36 nm), by using a sufficiently high electric field applied to a liquid surface.

1.2.3. Emulsion Droplets

Emulsions are heterogeneous systems formed by two immiscible phases in such a way that one phase is dispersed into the other as droplets of colloidal size. They can be classified according to the size of the droplets into macro-emulsions (with a droplet size >1 μm) and miniemulsions (also called fine-emulsions and nanoemulsions[42], with a significantly smaller droplet size, between 100 and 1000 nm). To avoid the coalescence of the emulsions, it is necessary to add surface active materials (emulsifiers) that give rise to a stabilization effect due to steric, electrostatic, or electrosteric mechanisms. Therefore, the main problem is to produce monodisperse nanometer-sized emulsion droplets. Nowadays, this problem is solved by a high energy input, for example, by means of an ultrasonic treatment in combination with the addition of hydrophobes to overcome Ostwald ripening. In this way it becomes possible to produce oil-in-water or water-in-oil miniemulsions down to a droplet size of 100 nm.[43] A few authors have characterized microscopic and submicroscopic liquid droplets immersed in another liquid and deposited on a solid surface. In a very recent report, Zhang and Ducker[44] successfully applied tapping mode AFM to observe very small interfacial oil nanodroplets of decane (height 2–50 nm) formed at the solid/liquid interface (hydrophobized Si wafer/aqueous ethanol-containing solution) by direct adsorption from an emulsion. The size and contact angle of the droplets could be varied by changing the concentration of ethanol in bulk (Figure 4). The authors justified this study because small interfacial droplets are largely unexplored and offer the opportunity to study the effects of size on the properties of matter. These nanodroplets were thought to be formed from a bulk emulsion and by a subsequent deposition, that is, they are not the remains of previously deposited larger droplets. This was evidenced by dynamic light scattering, which showed that droplets existed in the bulk and that the

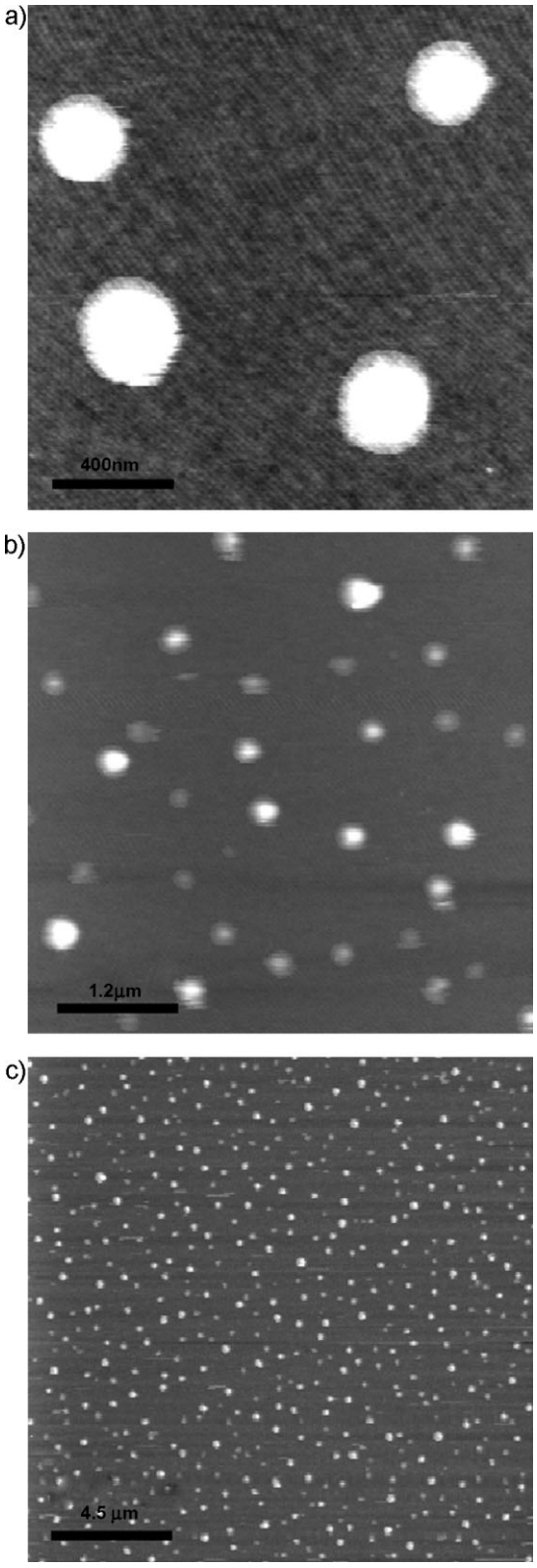

Figure 4. AFM tapping-mode images of decane droplets at the interface between OTS-modified silicon and decane dispersed in 25% ethanol aqueous solution. Reproduced with permission from Reference [44]. Copyright 2008, American Chemical Society.

volume distribution was similar in bulk and at the interface. In an earlier report,[45] these authors described the formation of very thin interfacial oil droplets by sequentially exposing a hydrophobic Si wafer to two solutions of decane, where one solvent was a poorer solvent than the other. The decane droplets had spherical cap shapes and displayed diameters of approximately 1–10 μm and maximum heights of about 10–500 nm. They hypothesized that this method of decorating interfaces with droplets is quite general, and that the method may be useful for the controlled modification of interfaces, but that inadvertent application of the method may lead to unanticipated interfacial properties. Gunning et al.[46] were able to image larger micrometer-sized oil (tetradecane) droplets in water on a polystyrene (PS) surface. While at low magnification the liquid surface appeared featureless, a close-up look showed the presence of concentric rings (Figure 5a), which were suggested to be caused by an optical interference effect, as we had previously described for these kinds of round-shaped objects having topographical contrast in the micrometer range.[47] Finally, Tongcher et al.[48] have reported that stable liquid nanodroplets (sizes between 180 and 630 nm) on a solid surface can be investigated by AFM using a miniemulsion, the oil phase consisting of E7 (liquid crystal) and hexadecane as a hydrophobe dispersed in the water phase, stabilized with ionic and steric surfactants such as sodium dodecyl sulfate (SDS).

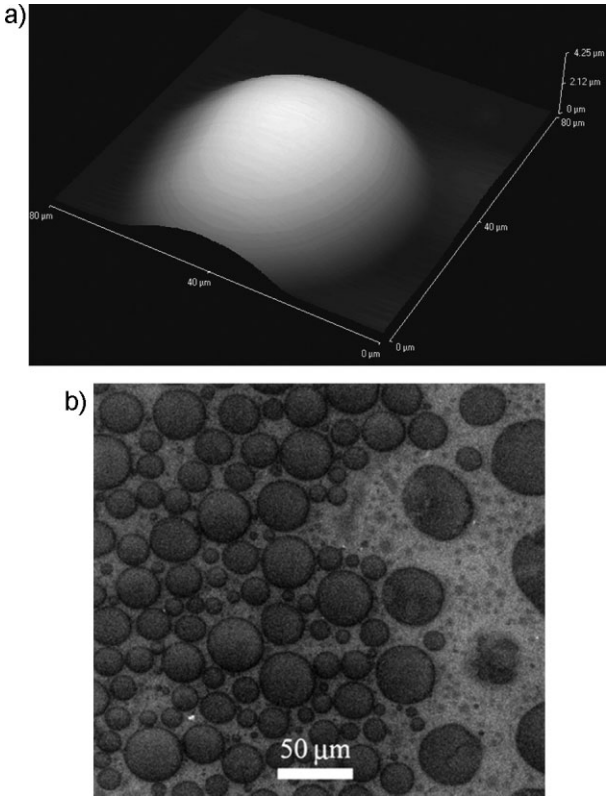

Figure 5. a) AFM image of a tetradecane droplet in water. Reproduced with permission from Reference [46]. Copyright 2004, American Chemical Society. b) Oil-in-water emulsion by ESEM. Reproduced from Reference [50].

Environmental scanning electron microscopy (ESEM) has been also successfully applied to the study of oil-in-water emulsions,[49] but oil droplets are observed at the liquid/vapor interface in this case, and resolution rests in the micrometer range. In Figure 5b we can see a protein-stabilized oil-in-water emulsion containing populations of both large and small oil droplets (approximately in the range from 100 nm to 50 μm).[50] In a later study, Mathews and Donald studied the conditions for obtaining morphological images of emulsion droplets using ESEM.[51] They obtained images of a variety of liquid systems containing micrometer-scale and smaller features. The limits of resolution were determined by sample motion and by beam damage effects; under optimum conditions, a resolution of a few tens of nanometers was obtained, higher than that achieved by conventional and confocal optical microscopy.

1.2.4. Condensation in Environmental Chambers via Heterogeneous Nucleation

The methods mentioned above permit the creation of micro- or nanoscale-deposited droplets. Now we will deal with nucleated droplets that are produced by in situ nucleation/condensation from the vapor phase. In contrast to homogeneous nucleation, which usually needs a several hundred percent RH, heterogeneous nucleation implies nucleation onto small structural or chemical heterogeneities, and can occur at RH just above 100% or below in the case of wettable heterogeneities. This way of producing small droplets allows one to change the concentration of the vapor phase to be condensed. This approach seems especially interesting for the study of systems that are not flat or homogeneous for a macroscopic droplet, but that can be ''seen'' as flat or homogeneous by a small (smaller than the roughness or heterogeneity scale) condensed droplet. It ensures that drops are in thermodynamic equilibrium with their vapor phase. In the case of AFM, concerns about the potential harmful effect of the vapor condensation on the electrical components of the AFM setup have arisen. However, this is currently a solved issue and commercial AFM firms offer setups with a total isolation of scanner and electronic parts from the environmental chamber. Therefore, imaging under reactive conditions without exposing the instrument to potential damage from the sample environment is possible. Using this approach the size of the condensed liquid structure can be tuned by changing the vapor pressure inside the chamber. Then, imaging of nanoscale droplets of even volatile liquids is allowed. Evaporation of nucleated droplets can be monitored by AFM by removing liquid from the reservoir or by slightly lifting the cantilever holder (Figure 6).[52] This will be further treated in the AFM section. The vacuum chamber of an ESEM can be used as environmental chamber, and nucleated water droplets can then be imaged. For example, in a recent report Aronov et al.[53] used an ESEM chamber for nucleating both microscopic and submicroscopic water droplets. They controlled the humidity in the chamber by raising the pressure in small steps while imaging the formation of small droplets. This will be further treated in the ESEM section. It would be interesting to study possible differences between wetting properties of a chosen liquid droplet created by direct

NANO MICRO small

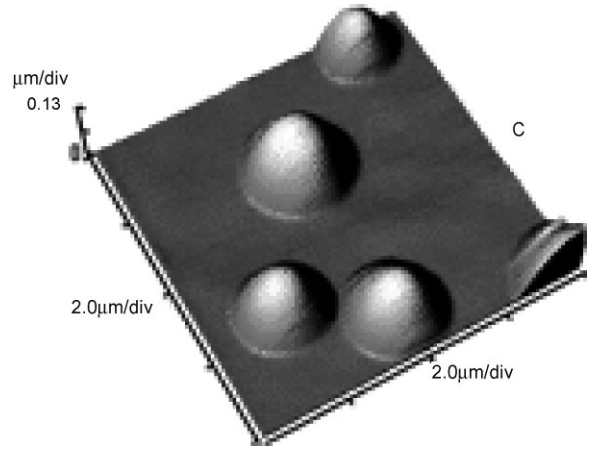

Figure 6. AFM image of liquid nanodroplets. Reproduced with permission from Reference [52]. Copyright 2006, American Chemical Society.

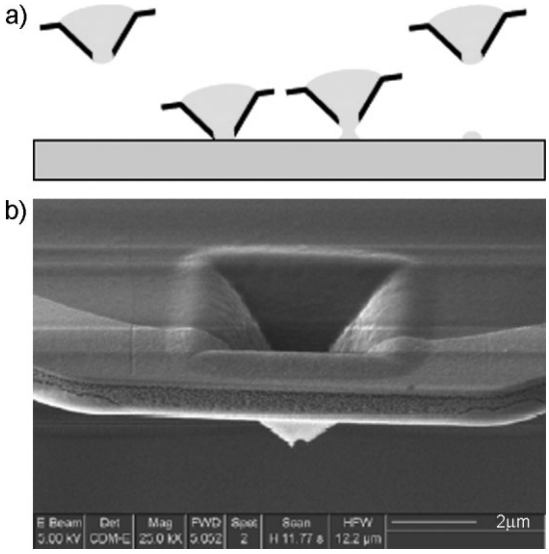

Figure 7. a) A conceptual sketch of nanoscale dispensing. b) SEM micrograph of a nanodispenser. Reproduced with permission from Reference [1]. Copyright 2005, A. Meister.

deposition or in situ nucleation. This is justified as sessile droplets are known to exist usually in metastable states (not at an absolute minimum energy configuration), while nucleated droplets most likely adopt a minimum energy state. To our knowledge, these kinds of studies do not exist in the micrometer or below range, but they do exist for macroscopic droplets, which adds further motivation. Lafuma and Quéré[54] observed a Wenzel state for a drop formed by condensation on a triangular spike-type superhydrophobic surface, but a Cassie–Baxter state when the droplet was deposited on the substrate. Furthermore, the contact angle hysteresis was much larger after condensation (110°) than that after deposition (5°). More recently, Narhe and Beysens,[55] working with the same type of surface, observed a contact angle of 111° for nucleated Wenzel-type droplets, and 164° for deposited droplets. Testing this at a micrometer scale has the difficulty of getting micrometer-scale sessile droplets reliably imaged without any significant influence of evaporation. In fact, most micrometer-sized droplets reported in the literature are water droplets that have been created by nucleation in an ESEM chamber.

1.2.5. Contact Methods: Ultrasmall Volume Dispensers

Special AFM cantilever/tip ensembles can be also used to form nanodroplets of reproducible size on a substrate by direct contact (capillarity). The newly developed nanoscale dispensing system (NADIS) is based on the transfer of liquid from a hollow AFM tip through a small opening at its apex to the substrate by direct contact (Figure 7), whereby droplets with femtoliter to subattoliter volumes can be deposited onto substrates with high spatial density. The transfer of liquid is controlled by the aperture size and surface energies. This system has proved able to deposit small droplets of glycerol with volumes down to 5 attoliter per droplet and spacing <500 nm.[56] This experimental setup has been recently applied by Jung and Bhushan[57] to deposit micro- and nanodroplets of a glycerol/water mixture on different surfaces. After that, the contact angle of the droplet was determined by measuring and analyzing the contact diameter, thickness, and volume of the droplet with an AFM. A rhodamine complex acted as a marker for the deposited droplets after complete evaporation of the solvent (typically a few seconds for submicrometer droplets). The obtained contact angle results were compared with those of a macrodroplet (2.1 mm in diameter). It was found that the contact angle on various surfaces decreases with decreasing the droplet size. Fang et al.[58] recently showed that tips with aperture diameter of 35 nm were able to deposit nanodroplets of glycerol-based liquids with diameters down to 70 nm (i.e., volume of 90 zeptoliter) and form regular arrays on silica surfaces with different hydrophilicities. Fine control of the droplet volume was also possible. The authors explained how by scaling down liquid manipulation, NADIS could provide a unique tool to probe wetting processes at the nanometer scale, a question that remains largely unanswered. Recently, Bruckbauer and coworkers have shown that double-barrel pipettes operating under scanning ion conductance microscope (SICM) control in an organic medium can be used to controllably deposit water droplets on surfaces.[59] To ensure longevity of the water droplets, presaturation of the organic liquid with water was found to be of paramount importance, because this prevents the slow dissolution of the water droplet into the oil medium. They managed to create drops of diameters ranging from 230 ± 140 nm (a few attoliters of volume) to 4.9 ± 0.1 μm (several hundred femtoliters). With the aim of depositing femtoliter droplets, Saya et al.[60] incorporated an in-plane nanotip into a microchannel at microcantilever tips. Droplets of water/glycerol with a diameter of 2 μm forming matrices with an interspot distance of 10 μm were achieved. It was demonstrated that the size of the droplet is significantly affected by the wettability of the nanotip surface and the substrate.

These scanning probe microscopy (SPM)-based strategies for dispensing of such ultrasmall volumes of liquids[61] will benefit from recent advances in AFM setups,[62] which allow

the independent control of two different AFM tips, one for depositing and one for imaging.[63]

1.2.6. Contact Methods: Double Transfer Printing from a Macroscopic Droplet

Another interesting way to form small droplets from an initial millimeter-sized droplet is called double-transfer printing. Recently, Gupta et al.[64] reported a technique to print small volumes of liquid on a hydrophobic substrate based on the repetitive contact of two surfaces, one of them initially portraying a macroscopic droplet. In a simple two-step procedure, discrete small volumes (≈70 femtoliter) of different liquid inks were printed on a polymer surface by using initial droplets with volumes around 10 μL. Recently, Uemura et al.[65] employed a simple technique using thin optical fibers for picoliter droplet collection and deposition onto a solid surface. Reproducible (coefficient of variation of 0.7%–2.3%) picoliter volumes were generated by retracting fibers from an aqueous phase immersed in an inert fluorinated immiscible liquid (to avoid evaporation). The fiber diameter and wettability were found to be dominant factors influencing final droplet volume, with no influence of the retraction speed. A critical contact angle between 60° and 75° was found to exist governing the droplet collection volume. The authors suggested that even smaller aliquots (attoliter to femtoliter volumes) could be reached considering the existing submicrometer diameter of optical fibers already available.

1.3. Imaging of Microscopic and Submicroscopic Droplets

1.3.1. AFM Imaging of Liquid Surfaces

AFM is the best-suited technique for imaging liquid droplets and films of micrometer and submicrometer dimensions on flat substrates due to its nanometer-scale resolution and capability of operating in ambient air or in any kind of controlled fluid (either gaseous or liquid) environment. In this section we will review the main characteristics of the imaging of liquid surfaces using AFM.

Two main AFM imaging modes are appropriate to image surfaces as deformable as liquid surfaces: noncontact AFM (NC-AFM) and intermittent contact AFM (IC-AFM, or tapping mode), both of them belonging to the general category of dynamic AFM (dAFM). The simplest AFM imaging mode, contact mode, is unable to track a liquid surface (Figure 8). If the cantilever experiences only long-range van der Waals interactions, the imaging is done in NC-AFM.[52,66] If, in addition, the tip periodically touches the surfaces, sampling repulsive and attractive forces, the imaging mode is called IC-AFM. As switching between both modes can occur easily, low oscillation amplitudes (<10 nm) and high quality factor Q (peaky characteristics of the resonance curve) cantilevers, with superior sensibility to weak forces, are preferred for stable NC-AFM imaging (Figure 9).[52,67]

An AFM tip interacting with a surface will always reduce its oscillation amplitude upon approach, and this behavior is independent of the physical origin (electrostatic, van der Waals, or chemical adhesion) or nature (short- versus long-range interactions).[68] The force exerted depends on the free amplitude (A_{free}), the tip-apex radius (which is not always well-defined or measurable), the amplitude chosen to run the feedback, and the imaging regime.[68] To probe soft samples in a nondestructive manner, forces well below 1 nN are required, and for this very small oscillation amplitudes ($A_{free} \approx 5$–10 nm) and sharp Si tips (radius ≈ 2–5 nm) must be used.[68]

In NC-AFM imaging mode, the AFM cantilever/tip is brought close to the surface while vibrating at a frequency slightly above (≈100 Hz) the normal resonance frequency of the cantilever, and at a certain amplitude (A_{free}). The sample force field induces a reduction in the oscillation amplitude compared to A_{free}. The cantilever is approached to the surface until the amplitude has decreased to a preset value (set-point amplitude, A_{sp}) due to the long-range attractive forces. This set-point amplitude is kept constant through the whole scanning by the feedback system. Since sensing is based on long-range weak forces, there is no physical contact with the sample. The disadvantage is that as it is based on long-range forces, it suffers from a reduced spatial resolution. In addition, since every surface exposed to air is covered by an adsorbed fluid layer, this can be a source of instability due to the formation of capillaries between the surface and the tip. This makes true NC-AFM rather difficult to achieve in air. To

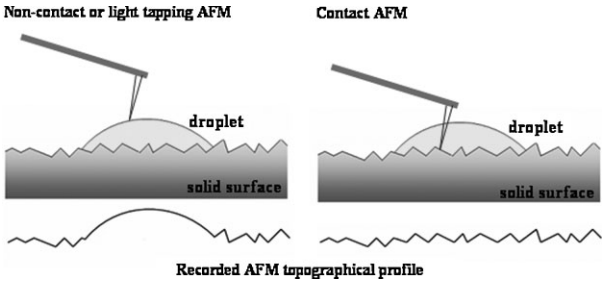

Figure 8. Schematic picture of an AFM tip scanning a surface with a liquid droplet in dynamic AFM (a), and in contact-mode AFM (b).

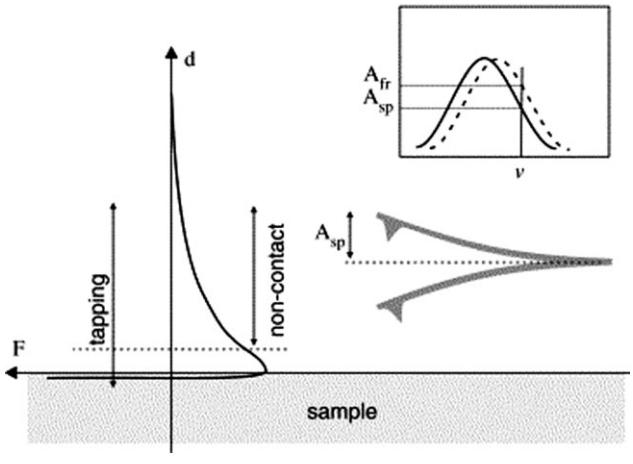

Figure 9. Essential principles behind dAFM imaging. Depending on oscillation amplitude and distance of approach the cantilever/tip ensemble is maintained within the long range tail of the attractive surface potential (NC) or it can periodically experience short range repulsive forces (IC or tapping mode). Reproduced with permission from Reference [70]. Copyright 2006, Elsevier Science.

NANO MICRO small

achieve stable drop profiles, A_{free} has to be lower than 10 nm to avoid any tip capture and $A_{sp} \approx 0.9A_{free}$ for sensitivity. The NC regime is maintained in a narrow A_{sp} range, and decreasing A_{sp} makes the tip further approach the surface, thus increasing image resolution, but also increasing the risk of accidental switching to the IC regime. General recommendations are to use a high spring constant k, which helps maintain stable imaging conditions when using small amplitudes, to choose driving amplitudes that keep a small value for the oscillation amplitude at resonance (ideally the actual amplitude will be smaller than 10 nm), drive frequencies 100 Hz higher than the resonance frequency, a precise location of the resonance frequencies, and to minimize as much as possible the scan rate.[69]

In IC-AFM imaging mode, the cantilever/tip vibrates with typical oscillation amplitude $A \approx 10$–100 nm or even higher at frequencies in the high kHz range. The damping of the vibration amplitude due to the interactions with the substrate serves as a feedback signal. Contact between the tip and the sample is produced during a very short time (1 μs) per oscillation, and this short contact time may reduce substantially the possible profile distortion.[31] Pompe et al.[31] showed the impact of the set-point amplitude A_{sp} on the profile (Figure 10a). For light tapping ($A_{sp} \approx (0.9$–$0.95)A_{free}$), good profiles were obtained. When decreasing A_{sp} (hard tapping), spurious jumps occurred and irregular profiles were obtained. A further reduction again provided stable profiles, but these were very different from the first ones (higher contact angle). This was shown to be due to a permanent liquid bridge, which is absent in the first case. This influence of the effective force exerted by the AFM probe onto the liquid surface was also investigated by Zhang et al.[44,45] for oil nanodroplets created at the solid/liquid interface by direct adsorption from an emulsion. The cross section of a single nanodroplet as a function of tapping-mode set-point is shown in Figure 10b (a smaller set-point corresponds to a larger applied force). The droplet is very deformable under the imaging force: both the height and the contact angle decrease with increasing imaging force. Drop shapes obtained under a small force were well-described by a spherical cap geometry, but they lost their shape when imaging using higher forces. Under such a high force, the droplet shape resembles something like a fried egg, with a thin plateau around a taller but flattened central section. Eventually, such a high force could be used to break or displace the whole nanodroplet. The effect of imaging conditions on the liquid profile was also studied by Wang and Kido.[27] They observed that the contact angles increased with an increase of the attractive forces from 0.13 to 0.50 nN, and the value at 0.13 nN was especially lower. Since the contact angles from the four sides of the droplet were different, which is a result of the scanning rate and direction of the tip, they proposed that the average of the contact angles from at least four such sides was necessary to get a reasonable value.

This process of formation/rupture of a capillary meniscus during each cycle and its influence on the imaging mechanism is not fully understood.[70,71] Due to the high oscillation frequency, the contact times are very short (μs) and can be controlled by altering either the tip–sample proximity or the oscillation amplitude.[72,73] The relatively high amplitude used in IC-AFM would provide the cantilever with enough kinetic/potential energy to overcome adhesive or capillary forces. Currently, the optimization of imaging parameters is rather a trial-and-error process.

There are several strategies for trying to minimize the risk of accidental bridge formation between the AFM probe and the liquid surface being imaged, including lowering the temperature and changing the surface chemistry of the AFM tip. Very recent results show that the formation of a liquid bridge is a thermally activated process, which suggests that reducing the temperature should help decrease the risk of complete formation of menisci, which needs some finite time to form.[74,75] Also, increasing the scan rate could reduce the probability of meniscus formation. When the tip is moved slowly, there is time for a capillary to form, but when moved faster, the capillary does not have time to form. This could, however, make the imaging instable. Finally, the surface chemistry of

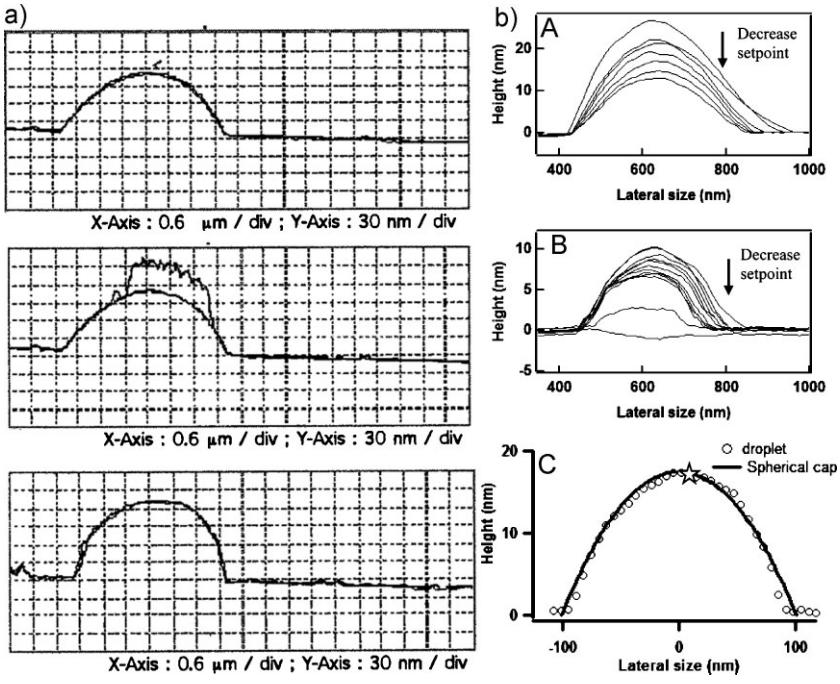

Figure 10. a) Line scans of the same liquid nanodroplet with different amplitude damping. Top: "light" tapping ($A_{sp} = 0.90$–$0.95A_{free}$); middle: set point amplitude reduced ($A_{sp} = 0.80$–$0.85A_{free}$); bottom: ($A_{sp} < 0.90A_{free}$). Reproduced with permission from Reference [31]. Copyright 1998, American Chemical Society. b) Profiles of a single interfacial decane nanodroplet at different AFM tapping-mode set points in 25% ethanol solution. Top: high set-points; middle: low set-points; bottom: cross section through the apex of the droplet at low force compared to an arc of a circle. The star shows the position of the center of droplet. Reproduced with permission from Reference [44]. Copyright 2008, American Chemical Society.

the AFM probes can also be tuned to minimize the wetting of the AFM tip by the probed liquid, thus helping to make the imaging process stable. Depending on the chemical nature (polar/apolar) of the liquid to be imaged, the surface of the AFM probe can be conveniently functionalized. It is best to render the surface of the probe polar/apolar if the liquid to be imaged is apolar/polar. Protocols to modify the surface chemistry of AFM probes are well-developed and intensively used by AFM researchers in a variety of fields. The reader is aimed at literature on chemical force microscopy[76,77] for complete details. For example, tips can be easily rendered polar with a surface coverage containing $-OH$, $-COOH$, or $-NH_2$ groups, or apolar with a surface coverage with $-CH_2$ or $-CH_3$ groups. As a proof-of-principle for how wetting properties of the tip may influence the stability of the imaging of the liquid surface, we highlight here the work by Wei et al.[78] in which the authors managed to image water layers on mica only when the tip was hydrophobized with a CH_3-terminated surface chemistry. Atomic resolution images of the mica surface were only obtained with this hydrophobized tip, as the (hydrophilic) raw tip formed liquid water bridges that made imaging unstable. The mentioned capillary bridges between an AFM probe and a solid surface can give rise to artificial liquid (nano)structures. They are real liquid structures, but are artificial in the sense that they have been induced by the imaging method. They have been observed as regular patterns of dots on mica[79] and Si wafers.[80] These authors proposed that these spots are condensed water produced at the tip–surface contact. If the tip moves at a high enough speed, the meniscus changes its angle between the AFM tip and the substrate, a phenomenon that was indeed previously observed directly.[81] At some instant/angle, the meniscus breaks, and a nanometer-sized water droplet, appearing as a spot in the AFM image, is left on the substrate. Larger islands can be formed by coalescence of various nanodroplets.

Recently, an attempt has been made to simulate the interaction of a liquid surface with an AFM probe using molecular dynamics (MD).[82] They demonstrated the hydrophobic nature of a Pt surface by obtaining an exact value of 115.4° for the contact angle of the water nanodroplet spreading on such a surface. They also investigated the contact angle offset caused by an AFM tip. Such an offset is predicted by MD to be due to the fact that the upper water molecules experience an attractive force provided by the tip.[82]

Finally, regarding time resolution of AFM, we note that taking stable liquid images usually takes about 15–30 min. This poor time resolution hinders the application of AFM for imaging small volatile liquid droplets, which evaporate before completion of an image, and also for accomplishing dynamic wetting studies (measurement of advancing and receding contact angles or following of dewetting processes). Eventually, video-rate AFMs would be excellent for these purposes.[83] Current developments are rapidly pushing AFM scanning speeds towards achievement of video-rates,[84] either through improvements in the control system[85,86] or with AFM cantilever/tips structurally optimized for high-speed scanning.[87] Therefore we expect them to play a role in making AFM not only a nanometer-scale spatial resolution technique suitable for imaging liquid surfaces, but also a high (ms) time-resolution tool that will allow dynamic micro-/nanowetting studies to be accomplished. As a final point, it is worthwhile to emphasize here that a small droplet observed by AFM after spraying a surface might not be the originally deposited one, but the remains that have stopped evolving/evaporating once most of the droplet profile lies within the range of actuation of long-range forces (1–20 nm in the case of a Si surface).[11,88] Indeed, most water droplets imaged under ambient conditions with AFM have maximum heights that fall within this range, even when conventional sprayers provide droplet sizes in the micrometer range.[89] It would certainly be interesting to design an experiment in which a remotely-controlled atomizer is activated inside an ESEM chamber (which does possess video-rate time resolution) once the convenient temperature and pressure are achieved, so that sprayed microscopic droplets could be imaged as-deposited. In general, to minimize this effect in the AFM imaging of liquid droplets, the use of liquids having low vapor pressure (for evaporation) and high surface tension or viscosity (for AFM sensing) is the best choice. The use of small environmental chambers is more convenient as they become saturated more easily.[52] Recently, a unique ''non-evaporation'' phenomenon, that is, an unusually slow evaporation process of sessile millimeter-sized droplets on hydrophobic alkanethiol self-assembled monolayer (SAM) surfaces has been reported using droplets containing a certain proportion of a volatile and a less-volatile component (alcohol/water binary mixtures). The non-evaporating phenomenon was characterized by the hours-long existence of the droplets maintaining constant contact angle, contact area, and volume.[90] It has not yet been exploited with microscopic droplets. ESEM has been proposed as a technique that could help to overcome the evaporation problem, but it works on a micrometer- rather than on a nanometer-scale and its high cost hinders its general availability in surface science laboratories. This will be treated further in the ESEM section.

1.3.2. ESEM Imaging of Liquid Surfaces

ESEM (or low-vacuum SEM) permits imaging of hydrated nonconductive samples[91] and is expected to be a promising tool for the study of wetting at micro-/nanoscales. For a complete description of the technique and its applications, the reader is directed to available specific literature.[50,92] Briefly, the main difference between conventional SEM and ESEM is that the imaged sample can be in a gaseous environment (instead of vacuum in SEM) up to a few torr (a few hundred Pa) of pressure and there is no need for a metallic coating for the specimen, as there is a mechanism for dissipation of the build-up charge. Accurate control of the sample RH can be achieved by changing the temperature and pressure. In the ESEM instrument, a series of pressure-limiting apertures (PLAs), which are discs with a hole drilled in the center, are placed down in the column and a pressure differential is maintained across each aperture. This configuration is called a differential pumping system. Vacuum is achieved at the electron gun at the top of the column. At the middle of the column, where the specimen is located, a relatively poor vacuum exists, which can be occupied by a variety of gases, such as water, helium, argon, or nitrogen. After inserting the

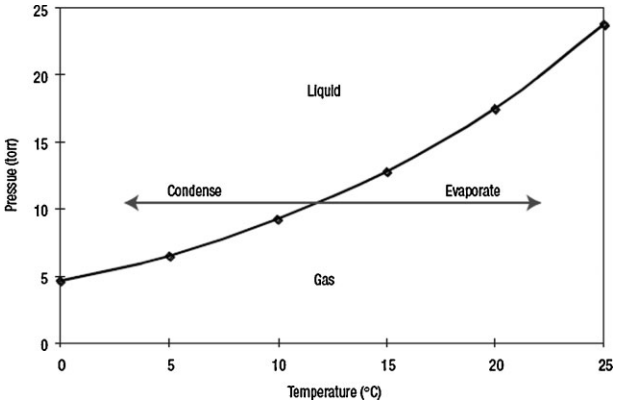

Figure 11. Saturated vapor pressure of water (100% RH) as a function of temperature in the relevant ESEM working conditions. Reproduced with permission from Reference [92]. Copyright 2005, Nature Publishing Group.

sample into the chamber, air at atmospheric pressure is replaced by water vapor at a pressure of a few hundred Pa. To maintain saturation conditions at room temperature, a Peltier stage is used to drop the temperature down to 3–5 °C (just above freezing) so that saturated vapor pressure can be maintained.[92] The Peltier or thermoelectric module is a small solid-state device that pumps thermal energy from one side to the other, where it is removed with the aid of a heat sink as current is applied. This permits the imaging of hydrated samples or even nucleated droplets. In case of low-vapor-pressure liquids such as oils, they can withstand vacuum conditions of a few hundred of Pa. In the case of volatile liquids such as water, the vapor phase must be kept in equilibrium with the liquid phase by carefully controlling the chamber gas pressure and the specimen temperature according to the phase diagram of water depicted in Figure 11. The resolution is lower than for metallic-coated SEM images. Time resolution is much better than AFM, and current ESEMs can output a high-quality video signal in real time, thus allowing dynamic in situ and in tempore studies to be performed.

Regarding the imaging mechanism, as the electron beam (primary electrons) collides with the surface, it causes the ejection of secondary electrons (SEs). These electrons collide with the water molecules, the most common imaging gas, ionizing them and providing the SE signal to the positively biased gaseous electron detector (GSED) through a cascade amplification process.[93] Since water molecules have lost electrons in this process, they became positively charged and attracted to the specimen, thus neutralizing the negative charge produced by the electron beam.[94] This makes it possible to image insulating (charge accumulating) samples without the use of metallic coatings.

Regarding the analysis of images, Stelmashenko et al.[95] presented a method to calculate the contact angle of droplets imaged with ESEM with the electron beam normal to the substrate (Figure 12). This has the advantage of not needing the surface to be tilted. It is assumed that the electron signal comes mainly from ''SE1''-type electrons, that is, electrons generated at the outermost sample surface layer due to the interaction between the electron beam with the specimen

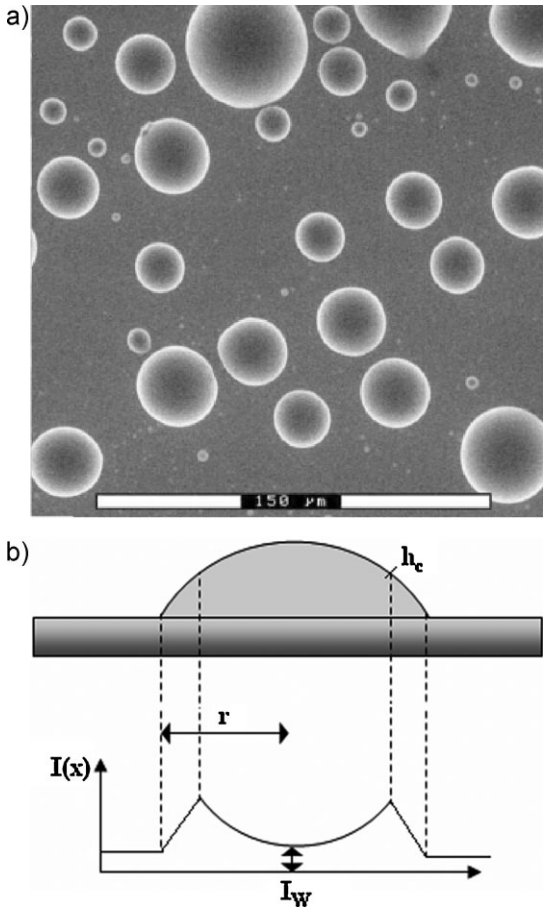

Figure 12. a) Images of droplets taken with the electron beam normal to the substrate. b) ESEM intensity profile across a droplet. Reproduced with permission from Reference [95]. Copyright 2001, The Royal Microscopical Society.

electrons, and that any other emission can be included in a constant background signal. The intensity at the top of the droplet is that of a deep horizontal layer of water, I_W. The non-uniform intensity arises from a differential emission of SEs due to the curvature (topography) of the droplet surface. Assuming the above, as well as a spherical cap geometry of the liquid droplet, whose topography can be expressed using Equation (2), the electron intensity (measured as a gray level in the image) across one diameter follows the equation

$$I(x) = I_{\text{backgr}} + I_0\left(1 - \frac{(x - x_c)^2 \sin^2\theta}{r^2}\right)^{-1/2} \quad (12)$$

With this information from the intensity across a diameter, we can directly measure r and x_c, and then it is possible to extract the value of the contact angle θ (when $\theta < 90°$), which is the only fitting parameter. The intensity coefficients I_0 (intensity of electrons from a flat layer of water) and I_{backgr} (the constant background intensity), as well as the value of I_W, should be equal for all large ($H > h_c$, where h_c is the cut-off height) droplets in the image. Having obtained the equilibrium value for θ, the droplet shape profile $z(x)$ (Equation (2)) can be

calculated for all droplets, large and small. These authors have reported a reasonable agreement with contact angles derived using the above model and those obtained directly from lateral views of the droplet profile.[95]

The availability of models to derive contact angles from images taken normal to the surface is important as it permits the measurement of the contact angles of all the droplets observed, irrespective of their location with respect to the sample edges. If the imaging is done parallel to the surface, then the contact angle can be measured by fitting the droplet profile to the appropriate function, but then only those droplets that are closer to the substrate edge can be used, as they interfere with the imaging of inner droplets. In spite of this limitation, this option could be preferred when direct electron irradiation of the substrate must be avoided. When the view line, that is, the electron beam, is not parallel to the surface, but is tilted at an angle α, Brugnara et al.[96] have shown that, assuming a spherical cap geometry, the real contact angle θ can be calculated from the inclination α and the projected contact angle ζ, using

$$\theta = 2\tan^{-1}\frac{\sqrt{\left(\tan\frac{\zeta}{2}\right)^2+(\cos\alpha)^2-1}+\tan\frac{\zeta}{2}}{\cos\alpha+1} \geq \alpha \qquad (13)$$

Of course, for $\alpha = 0^\circ$, $\theta = \zeta$. The equation cannot be used if the inclination angle $\alpha \geq \theta$ and if $\alpha \geq 180^\circ - \theta$.

Despite the enormous potential of ESEM in the study of microscale wetting properties of such a diversity of materials, it is necessary to understand that the absence of the metallic cover makes the surface more susceptible to radiation damage.[50] For instance, the formation of layers of water on a polypropylene surface enhances the probability of damage.[97] This is due to the fact that free radicals do not totally annihilate while receiving electrons coming from the primary beam.[98] Therefore a thorough assessment of the sample stability under electron irradiation is needed first to be engaged in experiments or interpreting results that might be affected by beam-induced artifacts. Of course imaging at high beam energy cannot be recommended because of the possible chemical and physical phenomena that might be triggered by the beam. For this reason, optimal scan rates should guarantee a proper image quality as well as the preservation of the droplet during the scan.[95] It is also possible that the use of bright electron sources such as field emitters might have potential in diminishing radiochemical and/or thermal effects, allowing operation at lower acceleration voltages.[51] Stelmashenko et al.[95] also suggested that the higher contact angle observed for water and glass (no differences were found with PS and silicon crystal surfaces) using ESEM could be due to the fact that the conditions in the ESEM chamber, such as low saturated pressure and charge effects on glass, could affect the balance of γ_{sv} and γ_{lv}, making wetting different from that in ambient atmosphere. The authors recommended further work to test this. Finally, a further technical challenge would be performing ESEM experiments at higher temperatures, and then at higher vapor pressures. This would allow a more direct comparison with macroscopic results that are often performed at room temperature. However, there are some fundamental constraints that have hindered these kinds of developments, mostly due to the fact that at such high pressures the efficiency of the amplification of the gas cascade signal diminishes. This is due to the fact that the mean free path and energy of the SEs become severely limited, and thus unable to overcome the water molecule ionization threshold (12.6 eV).[99] Additionally, as previously noted by Cameron and Donald,[100] working at the same temperature for both the vapor and the specimen would have the advantage of ensuring thermodynamic equilibrium, at which Young's equation (Equation 6) applies. A prototype SE detector that overcomes these limitations was built at the Cavendish Laboratory (UK) several years ago and a detailed report on its principles has been recently published.[101,102] It is therefore to be expected that this high-pressure/temperature ESEM will find interesting applications in the study of wetting properties at the microscale in the near future.

1.3.3. Other Techniques

We will include here some other works featuring the imaging of ultrasmall sessile droplets which are not of "general" use in the field (due to the limited resolution), but that merit attention.

Gu[103] reported the measurement of contact angles of silicone oil droplets with sizes ranging from the macroscopic to about 100 μm in diameter in water. Droplets were produced by a natural sedimentation process, and imaged using an optical microscope mounted with a CCD camera. From the variation of the contact angle with size, a line tension of the solid–oil–water system of 8.2×10^{-7} J m^{-1} was derived, which is close to those of similar solid–oil–air systems. The strong effect of the line tension on extremely small sessile oil drops (around 100 μm in diameter) on the hydrophobic solid surface in aqueous phase enables them to have nearly spherical shapes.

Using the sensitivity to the contact angle of the spectral drift observed upon laser irradiation in a electrowetting experiment of water droplets resting on superhydrophobic surfaces, Kiraz et al.[104] have recently proposed this method to indirectly determine the contact angle of droplets on superhydrophobic surfaces.

Sundberg et al.[105] have recently reported the use of confocal microscopy to the study of contact angles of micrometer-sized nucleated water droplets, and compared results with macroscopic (millimeter-sized) droplets (Figure 13). The method was developed for measuring both low (<30°) and high (30°–90°) contact angles. For droplets displaying low contact angles, the profiles could be reconstructed from the interference patterns in droplets condensed from the environmental water vapor, whereas for those displaying larger contact angles, for which it is not possible to resolve individual interference lines, a fluorescent dye had to be added to water, and droplets were then sprayed onto the surfaces and 3D image stacks were recorded and analyzed to measure the contact angle. By analyzing the dependence of the contact angle on the droplet size for microscopic droplets, an increasing contact angle was obtained at small radii, indicating a positive CLT with a magnitude ranging from $(3.2 \pm 0.4) \times 10^{-7}$ J m^{-1} to $(5.5 \pm 0.6) \times 10^{-7}$ J m^{-1}. The largest effect was usually observed below a 10-μm radius. Using the

NANO MICRO small

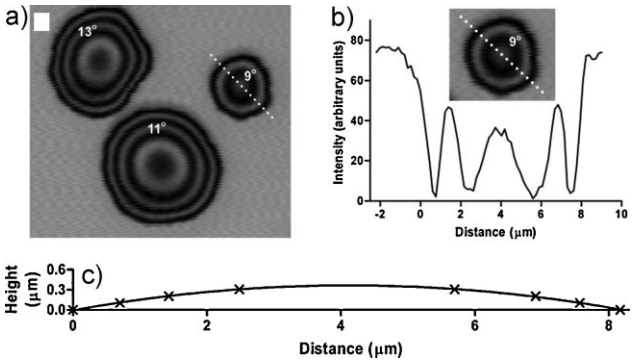

Figure 13. Interference method for measuring microcontact angles. a) Interference fringes in water droplets on ethanol-cleaned glass (image size $129 \times 115\ \mu m^2$). Contact angles indicated for the droplets. c) Drop profile with circular curve fitted to the data from the dashed line in (a). Reproduced with permission from Reference [105]. Copyright 2007, Elsevier Science.

interference data, the CLT varied between $(-4.6 \pm 1.7) \times 10^{-9}$ J m^{-1} and $(8.6 \pm 2.7) \times 10^{-9}$ J m^{-1}. The average contact angle of microscopic droplets with a radius $>10\,\mu m$ was not significantly different from the macroscopic contact angles.

Gorb et al.[106] have recently applied a cryo-SEM approach for visualizing droplets of various fluids (glycerin, water, lipids, and other biological fluids and their mixtures) deposited on biological and artificial substrates (Figure 14). As some biological fluids are often only available in small quantities, this approach has a huge potential for characterizing their physicochemical properties. After being sprayed with water, the cryo-SEM images of the upper surface of the peristome and the waxy inner surface of the pitcher of the carnivorous plant *Nepenthes alata* revealed water microdroplets on both zones, with an extremely high value of the contact angle (about 170°) over the waxy surface, whereas extended films were observed on the peristome. Differences in surface properties

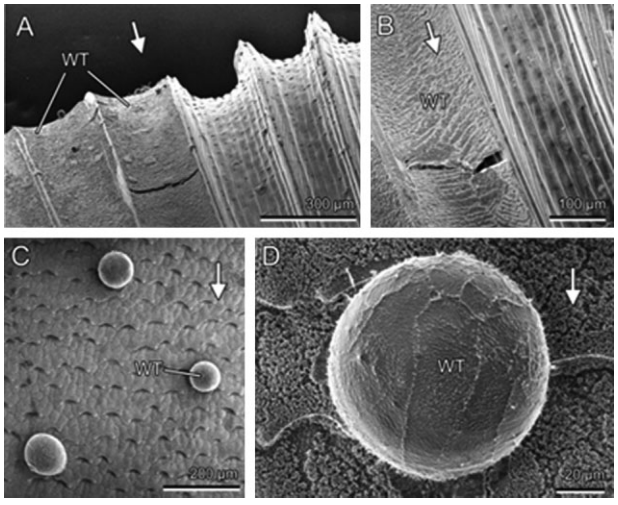

Figure 14. Cryo-SEM micrographs showing water (WT) droplets on the waxy inner surface of the pitcher of *Nepenthes alata*. Arrows show the direction to the bottom of the pitcher. Reproduced with permission from Reference [106]. Copyright 2007 Formatex.

are related to differences in the biological role of the different zones, such as insect attraction, retention, digestion, and uptake of nutrients.

2. Discussion

2.1. AFM

2.1.1. NC-AFM

Checco et al.[107] measured the contact angle of micro- and nanometer-sized alkane droplets partially wetting a model substrate (silanized Si wafers) using NC-AFM. The nature of the surface and the liquid used ensured minimal heterogeneity and pure van der Waals interactions. Since alkane droplets could not be formed under ambient conditions due to their volatility, the authors used a designed chamber that was connected to the AFM head. With this approach they could access contact angle values in a very broad range of spherical-cap-modeled droplet sizes, thus being able to measure the CLT with an unprecedented accuracy. The contact angle was found to decrease with decreasing droplet size from macroscopic scales. An important result of this work is that at a sufficiently high range of droplet sizes, the modified Young's equation (Equation (6)) does not correctly describe the experimental data, which authors ascribed to a paramount importance of surface heterogeneity, a hypothesis that was further supported by numerical simulations. In a more recent paper and also by using an evaporation–condensation chamber, these authors[70] measured the contact angle of ethanol nanochannels formed on a surface consisting of hydrophilic COOH-terminated and hydrophobic CH_3-terminated lines. Ethanol selectively wetted the hydrophilic lines with an apparent contact angle at the stripe's boundary of $12° \pm 1°$, a value significantly lower than that measured macroscopically for an ethanol droplet on an octadecyltrichlorosilane (OTS) surface ($30° \pm 1°$).

NC-AFM has been also applied to the study of the local wetting of human hair, which is an important system in beauty care science and whose behavior depends on its surface state.[108] Two different techniques were used depending on the nature of the liquid. For nonvolatile liquids, small drops of liquid were directly deposited on the solid by using a microsyringe, while for volatile liquids a condensation chamber was used. The critical surface tension (γ_c) of the hair surfaces was hypothesized to be 22 mN m^{-1}, and the nanoscale wettability behavior of different liquids of known surface tension was in accord with this assumption. Although for most of the liquids γ_{lv} is higher than γ_c, and should then partially wet the surface, no droplets were seen to nucleate. This was addressed by considering a competitive penetration, nucleation, and/or dewetting. More polar liquids such as water and glycerol did not appear to wet any region of the cuticle, although water was seen to penetrate into the bulk of the hair fiber. Hydrocarbons preferentially wetted the cuticle edges, which are more polar. In a more recent report, these authors used AFM to study changes in wettability of the cuticle when

different covalently and noncovalently bound fatty acids were selectively extracted.[109]

2.1.2. IC-AFM

Wang and coworkers[28,29] imaged sprayed water microdroplets on mica and different metal surfaces using IC-AFM. On mica, they observed water droplets with an average height of 7.1 nm and an average radius of 78 nm. The corresponding contact angle was 10.8°. They also used this imaging mode to observe water droplets on polished, air-oxidized, and water-immersed pure chromium, nickel, iron, and SUS304 steel surfaces. The morphologies of oxidized and water-immersed pure iron could not be observed because of the surface roughness. They concluded that the nanoscale wettability was higher than the macro-wettability, but reasons for this were not determined. When different surfaces were compared, lower macroscale contact angles corresponded to lower nanoscale contact angles. They pointed out that the influence of organic contaminants on specimen surfaces might be one of the reasons. In general, organic contaminants give rise to a higher surface hydrophobicity, and their distribution may be not uniform at the nano- and/or mesoscale. When droplets are obtained by condensation, as there should be areas with little or no organic contaminantion, water might be preferentially condensed in these areas, resulting in lower microscale-wetting contact angles. Along these lines, results by Checco et al.[107] also point to the influence of small surface heterogeneities as mainly responsible for the observed decrease in contact angle when droplets decreased from 2 μm to 200 nm. The idea is that the most wettable domains act as nucleation sites, so contact angle increases as the size of the droplets exceed the size of the domains. This is certainly valid for nucleated (not deposited) droplets. Recently, Moosavi et al.[110] have shown that the motion of a liquid nanodroplet near a chemical heterogeneity depends not only on the difference between the equilibrium contact angles on the two regions but, in particular, on the difference between the corresponding Hamaker constants. For this reason the motion is not necessarily directed toward the more wettable side. We have recently analyzed the hydrophobicity of silicon sheets at a mesoscopic level[111] by measuring the contact angle of water droplets sprayed onto the surface in an environment of high humidity (>80%) with sizes around 430 ± 100 nm using IC-AFM. A contact angle value of $7.3° \pm 1.2°$ was obtained from AFM images, while a value of 27.8° was obtained by goniometry. Fraxedas et al.[112] imaged nanoscale water droplets confined in molecular nanobeakers inside an environmental chamber. By mechanically perturbing the air/water interface using the AFM tip, they could derive a much higher value for the nanodroplet surface tension than the well-known value of 0.073 N m^{-1}, which was ascribed to the nanometer-scale involved. IC-AFM has been also recently applied by Missert and Copeland[113] to visualize nanoscale nucleated water droplets on aluminum and gold surfaces, which is important in understanding atmospheric corrosion of interconnects in microelectronic components. As corrosion occurs in areas where the protective layer is locally compromised through the interaction with water and/or other aggressive agents, it is necessary to understand how water interacts locally with the surface. For both gold and passive aluminum portraying a surface hydrocarbon layer at high RH, grain boundaries, triple points, and grains protruding slightly above the background provided sites for preferential nucleation. The surface structure of the passive aluminum surface was irreversibly altered upon contact with a high RH environment, and 2-nm-high nodules decorated the surface when the RH is subsequently reduced to a low value. However, in the absence of a hydrocarbon layer, no change was observed either at high RH or after reducing it to a low value. This result points to the strong influence of the surface hydrocarbon layer on the way aluminum interacts with humid environments.

Pompe et al.[31] used IC-AFM to determine the CLT from the topography of liquid droplets by applying either the modified Young's equation (Equation 6) or the effective interface potential method,[19,20] which gave similar results. In order to create liquid surface topographies with high contact line curvatures, the droplets were sprayed onto substrates with a stripped wettability pattern and left to equilibrate. Both the local curvature and the local contact angle could be obtained by retrieving line profiles from the microscope image. From these data, the authors found CLT values in the range of 10^{-11} to 10^{-10} J m^{-1}, which are lower than values reported by other authors.[17] Pompe et al. attributed this to the limited resolution of the microscopy techniques used (optical microscopy). Other authors have argued for the fact that the characteristics of the surface are far from the ones required for the model applied.[17] Mugele et al.[32] were able to image sprayed HEG droplets, ranging in size from 380 to 8 000 nm (Figure 15) on silanized silicon substrates under ambient conditions, as evaporation occurred with several hours. For droplets in this range, an average contact angle of 26° was obtained, differing only slightly with that obtained macroscopically (24°) using droplets in the range 1–3.5 mm. Based on their experience, they concluded that the size-dependence of contact angle frequently found in contact angle goniometry experiments is not attributable to the CLT. By analyzing the line profiles of the microscale droplets by AFM, they could derive an upper limit for the CLT of 10^{-10} J m^{-1}. The sign could be either positive or negative, due to measurement uncertainty. Zhang et al.[46,45] also reported very similar contact angle values for microscopically (AFM) observed decane-rich droplets and for macroscopically (goniometry) observed droplets (Table 1), so there was no need to infer the existence of a CLT from their measurements. If they ignored the macroscopic data and calculated the CLT from the size dependence of the contact line of only the microscopic droplets, the fitted value was $(8 \pm 4) \times 10^{-11}$ J m^{-1}. Another example of the use of IC-AFM for the imaging of nanodroplets is the work of Karis and Nayak,[114] who discovered a new type of contamination of magnetic recording slider disks when analyzing them with IC-AFM. This imaging mode was used to characterize liquid nanodroplets that are formed when hygroscopic airborne particles (cloud condensation nuclei) become deposited onto electrostatically charged magnetic recording disks in ambient conditions. The existence of these liquid-like and viscous nanodroplets was found to be the reason for the anomalous results obtained in earlier low-flying

NANO MICRO small

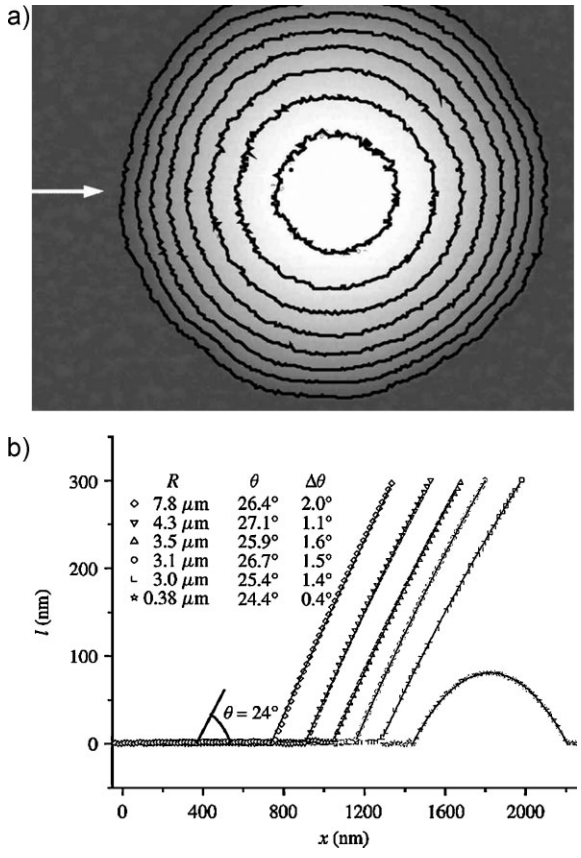

Figure 15. a) AFM image of an HEG droplet on phenyltrichlorosilane (PTCS)-coated Si ($R = 0.38\ \mu m$; $\theta = 24.4^\circ$). The contour lines are separated by 10 nm. b) AFM profiles for a series of HEG droplets with different radii. The solid lines are spherical cap fits. Reproduced with permission from Reference [32]. Copyright 2002, Brill Academic Publishers.

height sensitive friction and acoustic emission experiences.[115] Chemical analysis by time-of-flight secondary ion mass spectrometry (TOF-SIMS) revealed them to be mostly water coated with a thin film of lubricant. Connell et al.[116] used IC-AFM to measure the contact angle of oil droplets onto PS sheets. Small but constant values over a large number of droplets were obtained ($13^\circ \pm 2^\circ$), thus indicating homogeneity of the PS surface at the nanoscale. This illustrates another application of having contact angles characterized with such small droplets, that is, the investigation of the surface heterogeneity at very high spatial resolution. This capacity is indeed important as chemical heterogeneity is known to be one of the factors that influences macroscopic contact angle measurements jointly with surface roughness, which in contrast can be accurately described in a wide range of scales using AFM.[117,118] This is the same principle as that behind the microdroplet density assay (μdd), which can be used to study the homogeneity of a surface by recording the density of droplets formed upon exposure to saturated vapor environments using optical images.[119]

2.2. ESEM

ESEM microwetting studies have been carried out on both extended and particulate/fibrous solids. Stelmashenko et al.[95] performed fundamental studies on imaging of water droplets nucleated onto different standard surfaces such as hydrophobic PS and hydrophilic glass and silicon. They measured contact angles of micrometer-sized water droplets on these surfaces (Figure 16). They obtained a contact angle of $88^\circ \pm 5^\circ$ for PS, $51^\circ \pm 5^\circ$ for silicon crystal and $48^\circ \pm 5^\circ$ for clean glass. In the latter case, it is a much higher value than expected in ambient conditions. They found that the effect of the substrate was minimum for droplets of maximum cut-off height $h_c > 1\ \mu m$.

More recently, Brugnara et al.[96] measured the water wettability of poly(methyl methacrylate) (PMMA) and wax using small droplets imaged with ESEM (6.5 torr at $5.0 \pm 0.1\ ^\circ C$, 100% RH), and compared results with those obtained with the macroscopic static contact angle and vibrationally induced equilibrium contact angle (VIECA). PMMA was used because its surface composition is extremely pure and well-known and has a negligible roughness at the scales involved in the study. Wax is also an attractive material, as the roughness can be easily changed without changing the surface chemistry. ESEM, static, and vibrationally induced equilibrium contact angles were $66.4^\circ \pm 2.5^\circ$, $69.9^\circ \pm 1.6^\circ$, and $65.1^\circ \pm 1.5^\circ$ for PMMA, and $102.2^\circ \pm 6.3^\circ$, $108.1^\circ \pm 1.2^\circ$, and $104.1^\circ \pm 1.5^\circ$ for wax, respectively. A good correlation among the contact angles obtained by ESEM images and static and equilibrium contact angles was found, despite the drops condensed on the surface in the ESEM chamber often showing a nonspherical shape. A careful selection of the drops to be used was then necessary. The authors pointed out that the impact of this new approach is in resolving the problem of the size effect on the wettability properties of a material. In this particular case, no size effect is apparently present on these hard surfaces. It is noteworthy that the average value has a strong correspondence with the contact angle measured by the vibrational technique. Lau et al.[120] used ESEM for verifying whether the superhydrophobic properties of a surface they designed (vertically aligned nanotube forest covered with a thin layer of a hydrophobic polymer) was kept on the micrometer scale. For this purpose, water microdroplets were condensed onto the surface and successfully imaged. This allowed them to confirm that the superhydrophobic behavior was achieved down to the microscopic scale (Figure 17). Studying nanoscale aspects of fluid adsorption onto superhydrophobic surfaces is of the highest interest in the field. In a recent work, Cheng and Rodak[121] found that the lotus leaf exhibits superhydrophobic behavior if water drops of macroscopic sizes are placed on its surface, but that the lotus effect can vanish when water is condensed onto its surface from the vapor phase.

Recently, Jung and Bhushan[122] reported an ESEM study of the dynamic wetting of superhydrophobic surfaces consisting of a patterned silicon surface of cylindrical pillars covered by a SAM of a hydrophobic silane polymer. Contact angles on flat and patterned Si surfaces in an ESEM chamber at equilibrium and at increasing and decreasing condensation were obtained. The diameter of the water droplets used for the contact angle measurement was larger than $10\ \mu m$, so the size limit pointed out by Stelmashenko et al.[95] was avoided (Figure 18). For droplets smaller than $1\ \mu m$, a source of

Table 1. Compilation of published geometrical characteristics of microscopic and submicroscopic droplets imaged by AFM. The contact angle of their macroscopic counterparts is also given when available.

System studied	Maximum height [nm]	Base radius [nm]	Contact angle of microscopic droplet [°]	Contact angle of macroscopic droplet [°]	Reference
Water on pure Cr	6.7–21.1	25.6–42.9	44.2	76.8	[29]
Water on mica	3.93–9.78	45.2–127	10.8	31.4	[29]
Water on wet polished Cr	6.7–37.8	25.6–74.1	40 ± 10	80	[28]
Water on wet polished Ni	8.1–26	57.8–144.9	18 ± 2	72	[28]
Water on wet polished Fe	12.6–35.6	72.5–248	17 ± 4	68	[28]
Water on wet polished SUS304 steel	2.7–3.5	13.5–19.7	23 ± 4	70	[28]
Water on oxidized Cr	4.2–22.9	22.8–162.5	20 ± 5	70	[28]
Water on oxidized Ni	8.6–25.4	41.2–172.7	25 ± 6	62	[28]
Water on oxidized SUS304 steel	6.6–53.9	217.2–317.5	7 ± 2	70	[28]
Water on water immersed Cr	4.2–16.7	60.8–196.5	22 ± 10	60	[28]
Water on water immersed Ni	13.9–40.7	110.5–202.8	16 ± 4	68	[28]
Water on water immersed SUS304 steel	3–10.5	15.8–44.8	25 ± 8	68	[28]
Water on SUS304 steel	5.2–32.4	39.6–111.2	22.5	68	[26]
Water on naturally oxidized Si	11 ± 5	215 ± 50	7.3	27.8	[111]
Water on magnetic recording disk	73 ± 38	103 ± 36	67 ± 19	92	[114]
Ethanol on COOH-terminated surface	4–5	–	12 ± 1	30 ± 1	[70]
Octane on OTS surface		–	9 ± 1	8 ± 1	[70]
Hydrocarbon oil on PS	5–12	10–200	13 ± 2	14 ± 2	[116]
HEG on silanized silicon	–	380–8 000	26	24	[32]
Decane on OTS-Si in water	2–30	50–300	<10	<10	[44]
Decane on OTS-Si in ethanol aqueous solution (25 vol%)	2–30	50–300	15 ± 2	13 ± 2	[44]
Decane on OTS-Si in ethanol aqueous solution (25 vol%)	2–30	50–300	22 ± 2	18 ± 2	[44]

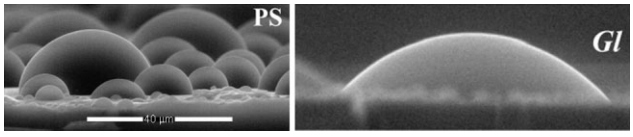

Figure 16. ESEM images of water droplets on PS and glass. Reproduced with permission from Reference [95]. Copyright 2001, The Royal Microscopical Society.

inaccuracy can be substrate backscattering. Static contact angles were measured once a dynamic equilibrium between condensation and evaporation was achieved. An advancing contact angle was measured while cooling the substrate (promoting condensation and drop growth), while the opposite was done for measuring the receding contact angle. The hysteresis angle could then be measured, and showed no difference when measured with micro- and macroscopic droplets. It was shown, however, to be dependent on the geometrical characteristic of the patterned surface, decreasing while increasing the distance between pillars.

Finally, another interesting, economically relevant, and suitable application field that merits specific attention is fibers, especially micro- and nanofibers (Figure 19a). ESEM has specific advantages for characterizing these solids as they have length scales in the micro- to nanoscale range in two directions, while being macroscopic in a third. In general, the performance of a fiber is strongly dependent on its wetting properties.[94] The evaluation of the wetting properties of fibers have been traditionally accomplished using the Wilhelmy technique,[123] in which the force between the fiber and a test liquid is measured upon contact. A major limitation of this technique relies on the uncertainty in the precise measurement of the fiber perimeter, especially in the case of microfibers. This technique also provides fiber-averaged results, so the use of small droplets could provide additional information at a sub-single-fiber level.[94]

Polypropylene (PP) fibers, one of the most important fibers in industrial textiles due to their excellent physical and chemical properties, are currently finding applications in oil-related fields as oil sorbents, oil coalescers, oil filters, and oil separators. Therefore, it is becoming increasingly important to obtain good knowledge on oil-wetting properties of these systems. These fibers are also creating much interest in hygienic and biomedical engineering. To be successful, they must have the ability to interact specifically with micrometer- and submicrometer-sized objects such as cells and proteins, a process that is known to be dependent on the substrate hydrophobicity. Thus, the biomaterial field is also expected to be benefited by the knowledge that ESEM can provide in this field.[124] We will now show how the fiber water and oil wetting properties can be accessed via ESEM.

Quantitative analysis of contact angles from the images requires the use of fitting functions, especially in the case of low contact angles, where the tangent method[125] can hardly be applied due to the meniscus curvature at the three phase contact line. In the case of droplet-wetting fibers (drop-on-fiber systems), Carroll's approach[126] must be used, which permits the calculation of contact angles of barrel-shaped droplets on cylindrical solids through an analytical expression relating the droplet length L, the maximum drop radius h_2, and

NANO MICRO small

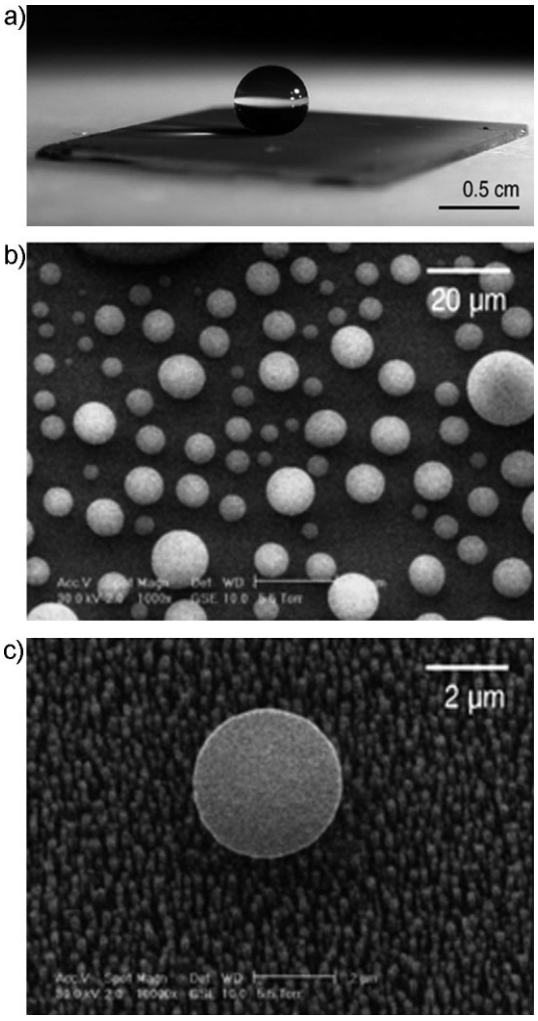

Figure 17. Water droplets on a poly(tetrafluoroethylene) (PTFE)-coated forest. a) Macroscopic droplet. b) ESEM image of micrometer-sized droplets. c) ESEM image of a single droplet. Reproduced with permission from Reference [120]. Copyright 2003, American Chemical Society.

the fiber radius h_1 (Figure 19b):

$$\frac{\overline{L}}{2} = aF(\varphi_1, k) + nE(\varphi_1, k) \tag{14}$$

where $\overline{L} = L/h_1$, $n = h_2/h_1$, and $a = (n\cos\theta - 1)/(n - \cos\theta)$. k and φ_1 are defined as $k^2 = 1 - a^2/n^2$ and $\sin^2\varphi_1 = (n^2 - 1)(n^2k^2)$, and $F(\varphi_1, k)$ and $E(\varphi_1, k)$ are elliptic integrals of the first second kind, respectively.

Wei et al.[124] carried out water and oil microwetting experiments using ESEM. Experiments performed by nucleating water droplets onto the fiber samples gave images showing droplets with high contact angles, which indicates the hydrophobic nature of the PP surface. In contrast, experiments carried out with oil microdroplets (which were added using a microinjector since oil condensation was not available), consistently showed the highly wettable character of the surface towards the oil (small contact angle). Quantification through Carroll's approach was undertaken by the same authors,[127] obtaining a contact angle of 15°–20°, demonstrating the affinity for oil, and 85°–95° for water. In a later work, the authors observed small but significant differences in the wetting behavior of three different oils of increasing viscosity.[128] Calculated contact angles were between 15°–25°, indicating the affinity of PP fibers for oil. Finally, these authors used ESEM to characterize the change in wetting properties of PP and polyethylene terephthalate (PET) fibers at the microscale upon (cold) plasma treatment, a process that does not modify bulk properties of even the most delicate materials.[94] After plasma treatment, the profiles of the water droplets are significantly altered on PP, displaying a lower contact angle and indicating a more hydrophilic surface (Figure 20). Droplets also lose their symmetry, which can be caused by the concurrent change in nanoscale topography as revealed by AFM.[129] Similar results were obtained in the case of PET fibers.[124] Using X-ray photoelectron spectroscopy (XPS), the authors correlated the change in wettability measured by ESEM with the surface composition. While carbon dominates the surface chemistry of the untreated PP fibers, as indicated by the (1s) peak at ≈285 eV, an oxygen-enriched surface is produced after plasma treatment, as evidenced by the appearance of an additional peak at ≈531 eV.

In a recent report, Carmody et al.,[130] guided by the need to find the most efficient material to be used as sorbents in oil/fuel spills, tested the surface properties of different materials (sand, clays, and cotton fibers). Wetting properties were characterized by using classical contact angle goniometry with 1 μL droplets of different test liquids (water and different oils). In the case of cotton fibers, which are mainly composed of cellulose, the authors also performed an experiment for imaging water and oil microdroplets on the fiber surfaces. Cotton wax may strongly interact with organic substances such as hydrocarbons through nonpolar interactions. The authors reported contact angle values of 145° and 10°–17° for water and oils, respectively, as measured with deposited sessile droplets. From ESEM images of microdroplets nucleated on single fibers, they reported corresponding values of 85°–95° and 15°–20°. While no reason for this difference is discussed, it is likely that in the case of water (liquid with no high affinity for the surface), the droplet is "seeing" a composite surface composed of air pockets and fiber surface, which, according to the Cassie–Baxter rule, should give rise to an augmented value of the contact angle. In fact, the surface is a network of fine fibrils giving rise to a complex porous structure, in which about 30% of the total volume is unoccupied.

Finally, we will present results for particulate solids, which have characteristic length scales in the micro- to nanoscale range in all directions. Their wettability characteristics are usually studied by using imbibition tests, which are time-consuming, indirect, and provide averaged results, so the microscopy approach has an interesting potential here. To illustrate this, we will focus on some results from the study of the wettability of oil field rocks. By using ESEM, Buckman[131] was able to nucleate water droplets onto these surfaces and to observe the contact angles between water and the mineral phases. High water contact angles indicate oil-wet conditions,

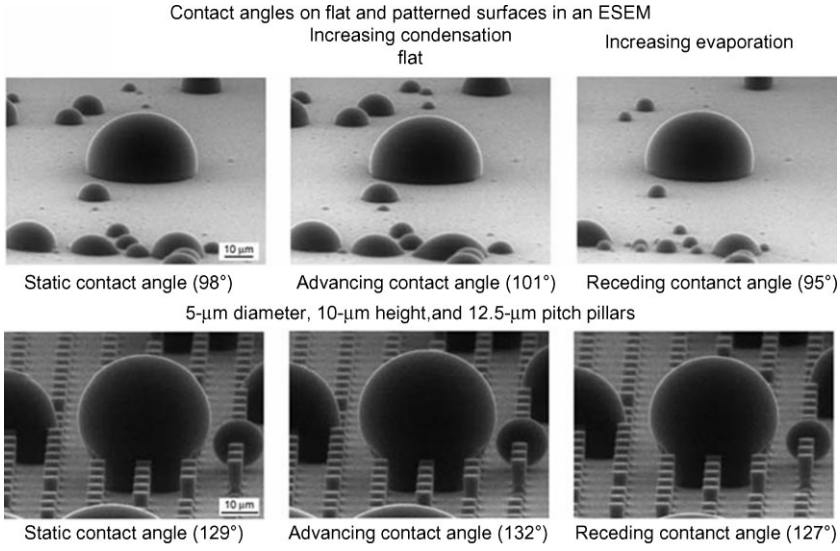

Figure 18. Static, advancing, and receding contact angles of water microscopic droplets onto flat and patterned Si surfaces in an ESEM chamber in equilibrium, increasing condensation and increasing evaporation, respectively. Reproduced with permission from Reference [122]. Copyright 2008, The Royal Microscopical Society.

while low contact angles indicate affinity to water (Figure 21). Images were taken at 5 °C to minimize the risk of accidental freezing, which may occur from local fluctuations in the temperature, and at a pressure of about 6–8 Torr. The author analyzed whole rock chips from a typical reservoir sandstone containing quartz grains and the clay illite. Water condensed onto the quartz formed low-contact-angle (<90°) droplets, indicating areas of high water affinity, while on the illite zones high contact angles were obtained (<90°), indicating oil-wet conditions. This illustrates how the technique permits differentiation among the different phases that comprise petroleum reservoir rocks. Similar work was carried out by Okasha et al.[132] to acquire microscopic information on the wettability of carbonate reservoirs, which is fundamental in the understanding of fluid flow in all aspects of oil production.

ESEM has been also used to measure the contact angle on the surface of porous solids. In this regard, it has recently been used to advance the performance of porous catalyst layers forming proton-exchange membrane fuel cells, a promising power supply for portable applications in the near future. The only chemical product of fuel cells is water and its transport properties are largely determined by the properties of the interface formed by the gaseous fuel, the liquid electrolyte, and the solid catalyst surface.[133] Imaging of the samples in wet state was conducted by cooling the sample down to 5 °C with a Peltier device in a water vapor at 7–9 Torr (Figure 22). The hydrophobicity at the micrometer-scale of three different polymers was studied and could also analyze the effect of degradation of the membrane electrode assembly after 700 h of use in a fuel cell. Local microscale contact angles were correlated with surface composition using energy dispersive X-ray spectroscopy (EDX), and hydrophobic porosity calculations were performed using independent mercury porosity determinations and measuring the relative volume of the hydrophobic pores from ESEM images (in this case, the pores larger than 0.1 μm are taken as the hydrophobic pores). The same authors later reported a study on the microwettability of three different catalyst layers formed by the same polymer and the same catalyst loading, but from different commercial firms, which therefore exhibit different microstructures and pore size distributions.[134] They pointed out that the real contact angle can hardly be detected by traditional equipments and that interface roughness causes water droplets to be nonsymmetrical. They could follow the growth of water droplets onto the surfaces investigated, thus allowing them to discriminate which droplets to use for the measurement of the contact angle.

Paper is another industrial system of interest that is porous and sorptive, which makes the measurement of its hydrophobic properties a non-trivial task. In fact, traditional contact angle measurements have not gained wide acceptance for these kinds of systems, as they have not shown to be able to explain the experienced production problems. The analysis is complicated by the fact that in many cases wetting and imbibition occur within the first seconds after the solid–liquid contact.[134] Liukkonen tried to study the wettability of different kinds of papers using ESEM and comparing the

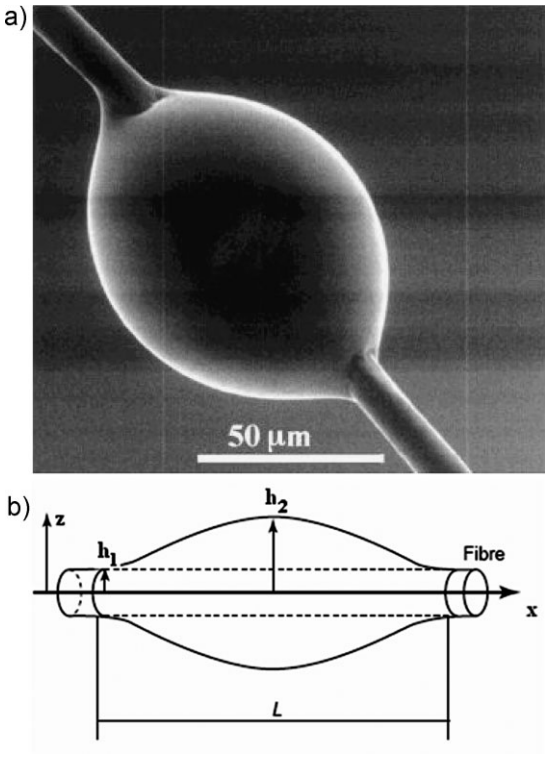

Figure 19. a) ESEM image of a textile fiber wetted by water. Reproduced from Reference [50]. b) Geometry of a barrel droplet on a fiber. Reproduced with permission from Reference [127]. Copyright 2002, Elsevier Science.

NANO MICRO small

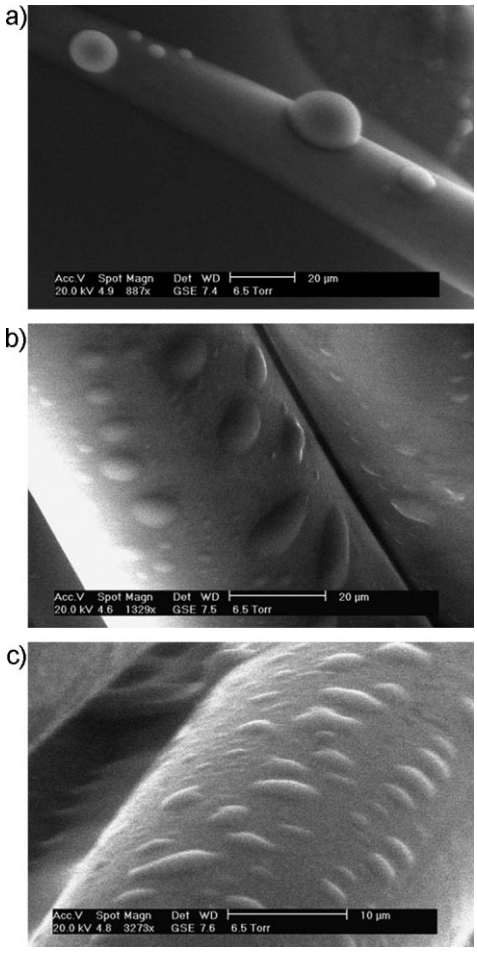

Figure 20. ESEM images of PP fibers: a) untreated; b) oxygen-plasma treated for 30 s; c) oxygen-plasma treated for 60 s. Reproduced with permission from Reference [129]. Copyright 2004, Elsevier Science.

results with macroscopic tests.[135] Sometimes, formation of drops was observed, while in other cases the water saturated the pores in the web structure. In general, they found that the macroscopic contact angle compares well with the advancing contact angle derived from the ESEM images. No appreciable size effect on wettability was observed in this case.

2.3. Wetting Patterns

In this section we will review the main achievements in the imaging of droplets onto surfaces to which a chemical or topographical micro- or nanoscale pattern has been imposed. Wettability patterns, especially those through the patterning of organic molecules, are currently one of the main trends toward molecular-scale devices.[136,137]

Irradiation of the surface is one of the used approaches. Aronov et al.[138] reported a hydrophobization of hydrophilic acid-cleaned SiO_2 surfaces upon irradiation with low-energy electrons (<500 eV), energies that are low enough to avoid the creation of defects and initiation of ion desorption. XPS confirmed that the hydrophobization is due to the formation of strongly hydrophobic and negatively charged alkyl (C–H) groups. More recently, these authors have proposed a

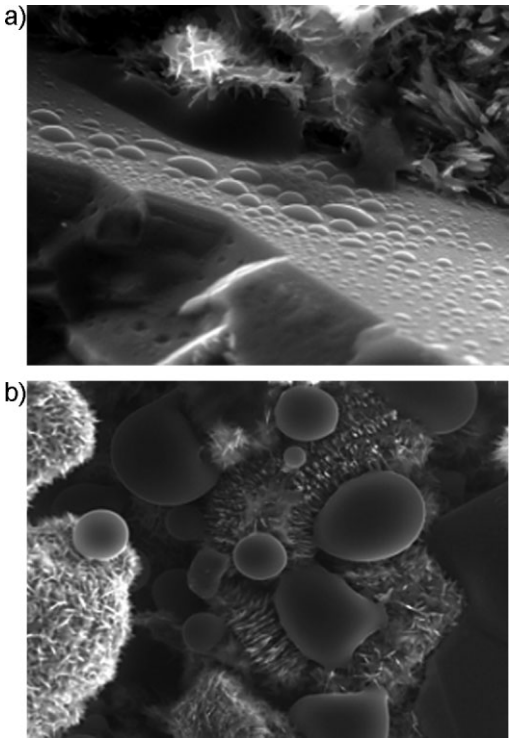

Figure 21. ESEM micrograph of water wetting of an illite-rich quartz sandstone reservoir rock. a) Quartz. b) Illite. Reproduced with permission from Reference [131]. Copyright 2008, FEI/Phillips.

complete theory to explain the observed decrease in wettability upon low-energy irradiation.[139] The higher hydrophobicity observed under electron irradiation by decreasing solid/vapor and solid/liquid interfacial free energies when reduction of the first is always lower ($\Delta\gamma_{sv}>\Delta\gamma_{sl}$) is explained by such a theory. UV irradiation restores the initial hydrophilicity. A broad range of materials have been shown to hydrophobize using this method, including *n*- and *p*-Si, SiO_2, S_3N_4, mica, Al_2O_3, glass, Al, and Ti metals, which are all coated with oxide films, and biomimetic materials (sea shells, hydroxyapatite, and related calcium phosphates). A combination of low-energy electron irradiation of a chessboard-type mask-protected SiO_2 with an ESEM device was used to create a wettability pattern and to observe water droplets on them. On the treated (hydrophobic) areas, highly axisymmetrical and small (≈10 µm) droplets formed, displaying an average water contact angle of 52°, while larger (≈60 µm) highly irregular film-like structures formed onto the untreated (hydrophilic) areas, displaying a 22° water contact angle. Corresponding values of water contact angles of 89° and 18° were obtained using millimeter-sized droplets. Estimations of the CLT of $\tau \approx -7\times10^{-10}$ J m^{-1} and $\tau \approx 3\times10^{9}$ J m^{-1} were obtained by investigating the dependence of the local contact angle versus the local contact line curvature on the hydrophobic and hydrophilic parts, respectively, values that were found to be within the theoretical limits. These authors were able to form open-air microchannels when a stripe-type hydrophilic modification was imposed on the SiO_2 substrate, an advance that they proposed to be of interest in the design of microfluidic systems.

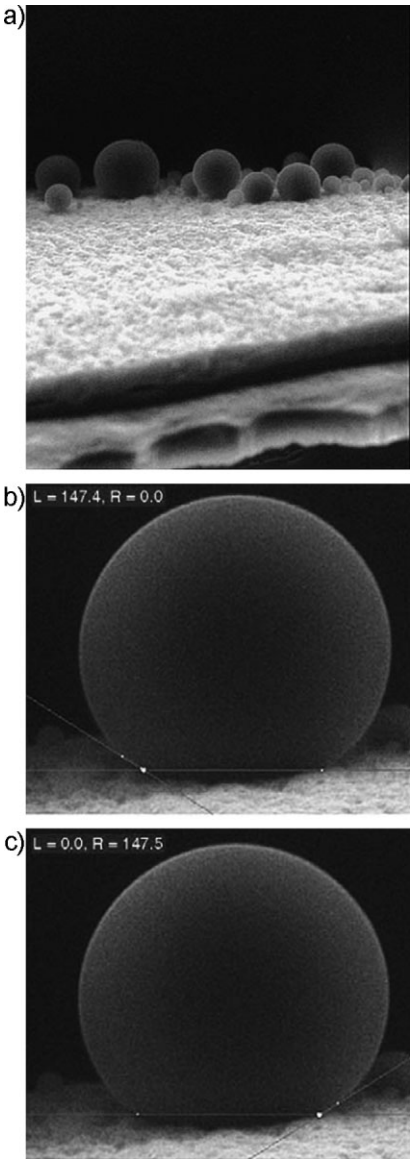

Figure 22. a) ESEM image showing microscopic water droplets condensed onto a porous catalyst layer. Note the asymmetry in the left- (b) and right-hand-side (c) contact angle. Reproduced with permission from Reference [134]. Copyright 2005, Elsevier Science.

Surfaces with micropatterned wettability were also constructed by Morita et al.[140] by photolithography of a hydrophobic fluoroalkylsilane monolayer on clean silicon. Stripes of varying widths from 1 to 20 μm were prepared. ESEM showed the water to condense preferentially in the Si–OH parts of the patterns, thus confirming the stripe-line hydrophilic modification of the surface. Condensation eventually resulted in the formation of liquid channels.[141] This micropatterning of the surface hydrophobicity was exploited to form 3D polymeric channels onto the surface, which could be imaged by AFM.

In a recent study, Léopoldès and Damman[142] provided a general route to macro- to nanostructuring using liquid droplets. As a substrate they used a gold-coated silica wafer functionalized with a homogenous hexadecanethiol SAM. Patches of this SAM were destructed using UV radiation through a mask in order to display either a chessboard or parallel line patterns, a procedure that produced a pattern of alternating hydrophilic (Au) and hydrophobic (CH_3) regions. When the surface was immersed in a bilayer consisting of an upper ethanol layer and a bottom viscous poly(dimethylsiloxane) (PDMS) layer, ethanol molecules diffused towards the bottom layer thus destabilizing the PDMS–substrate interface and creating droplets following a spatial arrangement that depended on the type of mask used. This gives rise to a 3D patterned liquid PDMS body that could be solidified after UV light irradiation.

Checco et al.[70,143] produced nanoscale wettability patterns using a biased AFM tip on a Si wafer that was previously hydrophobized by adsorption of an OTS monolayer. This was done inside an environmental chamber, which allows the control of vapor concentration and temperature. Applying a voltage between the metallic tip and the substrate, the authors were able to oxidize the terminal $-CH_3$ groups to a hydrophilic $-COOH$. The stripes created had only minimal topographical contrast (3–4 Å). The width of the stripes could be tuned by varying the applied bias voltage and the ambient humidity. The authors chose ethanol as the liquid to condense as it is volatile and completely wets the hydrophilic nanostripes. Additionally, ethanol does not wet the more hydrophobic OTS surface as was evidenced by a macroscopic contact angle of 30°. The morphology of the condensed liquid nanostripes was imaged in pure NC-AFM at different degrees of vapor adsorption (under-saturated, saturated and over-saturated, Figure 23). This was achieved by varying the temperature offset (ΔT) between the sample and the liquid reservoir (at 25 °C). At $\Delta T \approx 10$ °C, a small amount of vapor adsorbed onto the surface. At $\Delta T \approx 0.5$ °C (close to saturation), a ''visible'' amount of condensed liquid was evident, and at $\Delta T \approx -15$ °C, even more liquid became adsorbed, forming cylindrical channels. The process was fully reversible. At saturation, experimental results matched theoretical predictions using the modified Young's equation (Equation (6)) jointly with the density functional theory with an interface potential containing only dispersive molecular interactions.

Another approximation for building open microfluidic systems is using nonplanar topographies prepared by photolithographic methods, which permit the fabrication of topographically nanopatterned surfaces. This approach is based on the fact that liquids prefer to wet the wedges and grooves rather than planar surfaces, provided that the wettability of the surface by the liquid is sufficiently high.[144]

Fukuzawa et al.[145] used a negatively biased AFM tip to electrochemically oxidize an uncovered Si wafer. As silicon oxide has a lower density than silicon, the local oxidation produced nanoscale ridges. A nonvolatile polymeric liquid was then applied by dip-coating. Because of the apolar character of the liquid, van der Waals contributions governed the interaction between the liquid and the substrate. The liquid film thickness could be controlled with subnanometer resolution by adjusting the removal speed and density of the polymer solution.

Wettability of condensed fluids has been also investigated using AFM on microstructured (rather than nanostructured)

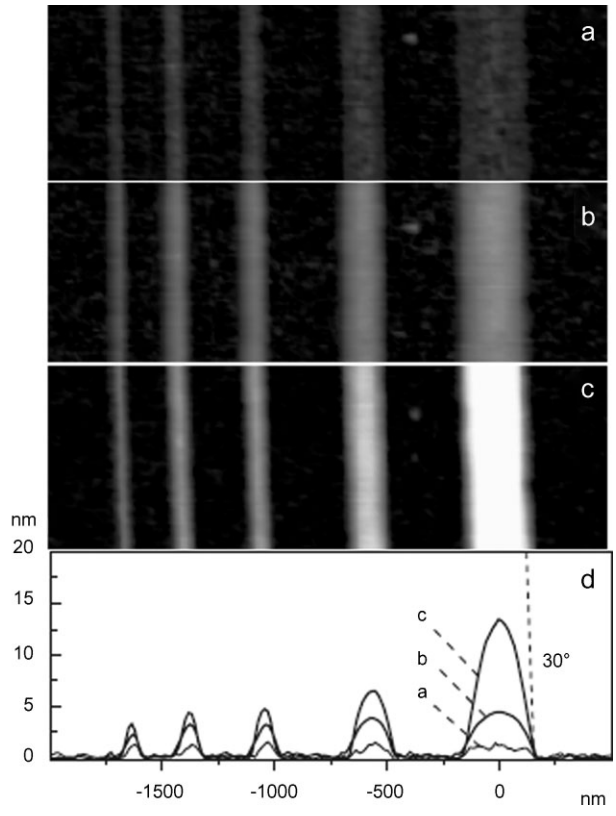

Figure 23. NC-AFM images of condensed ethanol onto hydrophilic stripes for ΔT equal to a) 3 °C, b) 0 °C, and c) −10 °C. In (d), the corresponding cross-sectional profiles are shown, where the dashed line represents the contact angle of ethanol on OTS, as measured macroscopically. Reproduced with permission from Reference [143]. Copyright 2003, American Physical Society.

surfaces. Seeman et al.[146] created grooves with rectangular cross sections in Si by photolithographic methods with depths between 100 and 900 nm, and widths between 400 nm and 3 μm. Despite the simplicity of the micro-/nanostructuring, a large variety of different wetting morphologies were observed using AFM. The liquid structures were created by exposing the surfaces to oversaturated low-weight PS vapors, and imaging by AFM was possible by lowering the temperature below the glass transition temperature of the polymer, thus ''freezing'' the formed liquid structures (Figure 24). The authors constructed a morphology diagram that depends only on the aspect ratio of the grooved geometry (ratio of groove depth to width) and the contact angle of the underlying substrate.

3. Summary and Outlook

The investigation of wetting properties of solid surfaces at a local scale is an emerging area in the field of surface science. It is still in its infancy and methods are being improved, but the potential that it offers to both fundamental and applied wetting research is recognized. It is indeed characterized by a highly disperse set of systems investigated and reported in a largely diverse set of scientific journals. We here provide an organized view of the state of the field, which should be useful for all those researchers wishing to explore new research routes. This review addresses both the achievements and the main limitations and problems associated. AFM and ESEM have been identified as the most relevant techniques currently used for imaging ultrasmall liquid surfaces. Both techniques are undergoing technical innovations that will strengthen their application in the field. In the case of AFM, we see that most of the results involve droplets that have lateral or vertical dimensions in the nanometer range, while those achieved with ESEM are mostly in the micrometer range. Large-area AFMs are not still generally available at surface science labs, but currently published results with large-area calibration surfaces make us optimistic about their application to laterally and vertically larger structures such as micrometer-sized droplets in the near future. In the case of ESEM, the use of field emitters is expected to play a role in diminishing beam effects, and will also push resolution to the nanometer range. This convergence between the two techniques could be very interesting for exploring the possible artifacts each might introduce. Time resolution is also important, as taking images in a short time (seconds), as in ESEM, helps avoid evaporation effects and allow performance of dynamic wetting studies. Common AFM requires at least about 15–30 min to acquire a stable image of a liquid surface, but there are current developments in both electronic and data acquisition systems, as well as in the design of AFM probes optimized for high-speed scanning (especially small cantilevers), that are rapidly pushing AFM towards video rates. As there are already successful reports in the biological field (monitorization of biomolecular processes taking place in the ms time scale), we expect that this advance

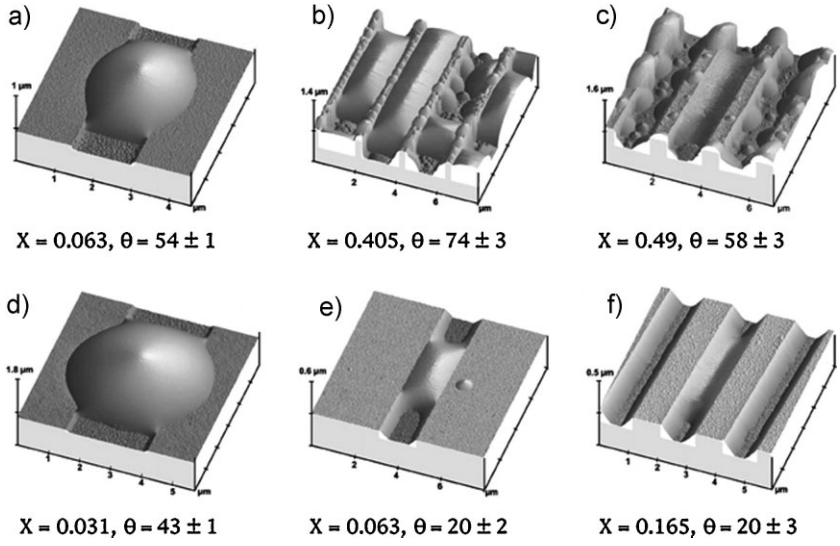

Figure 24. AFM images of liquid structures in grooves with rectangular cross section. Reproduced with permission from Reference [146]. Copyright 2005, National Academy of Sciences.

will play a significant role in the advancement of wetting studies at microscopic and submicroscopic levels. All these advances are expected to be important in the near future in the studies of a variety of phenomena discussed in the text, such as static and dynamic contact angles of droplets in the micrometer range and below, the patterning of liquid micro- or nanostructures onto surfaces (that could turn into patterning of solid micro- or nanostructures upon solidification), fundamental studies on nucleation and condensation of liquids onto surfaces, or even in other indirectly related fields such as the imaging of dynamical processes directly at fluid–fluid interfaces (instead of at solid–fluid interfaces after transfer)[147] at a very high spatial and temporal resolution.

Acknowledgements

Funding of our current research through grants from the Spanish Ministry of Science and Technology (Project MAT2006-12948-C04-03) and from Fundación Mutua Madrileña is gratefully acknowledged. M.L.G.M. acknowledges Junta de Extremadura and FEDER for a I3 Fellowship. A.M.V.: I would like to thank María José Nuevo Sánchez for giving me the possibility eight years ago to be engaged in research, which allowed me to do what I like most: exploring. I dedicate this work to her.

Keywords:
atomic force microscopy · environmental scanning electron microscopy · fluid interfaces · imaging · wetting

[1] A. Meister, *PhD thesis*, University of Basel (Switzerland) **2005**.
[2] M. A. Pacha-Olivenza, A. M. Gallardo-Moreno, A. Méndez-Vilas, J. M. Bruque, J. L. González-Carrasco, M. L. González-Martín, *J. Colloid Interface Sci.* **2008**, *320*, 117.
[3] Y. Liu, J. Strauss, T. Camesano, *Langmuir* **2007**, *23*, 7134.
[4] R. J. Emerson IV, T. A. Camesano, *Appl. Environ. Microbiol.* **2004**, *70*, 6012.
[5] N. V. Churaev, V. D. Sobolev, *Adv. Colloid Interface Sci.* **2007**, *134–135*, 15.
[6] L. Labajos-Broncano, M. L. González-Martín, J. M. Bruque, *J. Colloid Interface Sci.* **2003**, *262*, 171.
[7] L. Labajos-Broncano, M. L. González-Martín, J. M. Bruque, *J. Adhes. Sci. Technol.* **2002**, *11*, 1515.
[8] A. M. Gallardo-Moreno, M. L. González-Martín, C. Pérez-Giraldo, E. Garduño, J. M. Bruque, A. C. Gómez-García, *Appl. Environ. Microbiol.* **2002**, *68*, 2610.
[9] A. M. Gallardo-Moreno, E. Garduño, M. L. González-Martín, C. Pérez-Giraldo, J. M. Bruque, A. C. Gómez-García, *Colloids Surf. B* **2003**, *28*, 119.
[10] G. Kumar, K. N. Prabhu, *Adv. Colloid Interface Sci.* **2007**, *30*, 61.
[11] H.-J. Butt, D. S. Golovko, E. Bonaccurso, *J. Phys. Chem. B* **2007**, *111*, 5277.
[12] J. Drelich, *Colloids Surf. A* **1996**, *116*, 43.
[13] F. Rieutord, M. Salmeron, *J. Phys. Chem. B* **1998**, *102*, 3941.
[14] A. Milchev, A. Milchev, K. Binder, *Comp. Phys. Comm.* **2002**, *146*, 38.
[15] A. I. Milchev, A. A. Milchev, *Europhys. Lett.* **2001**, *56*, 695.
[16] T. Pompe, S. Herminghaus, *Phys. Rev. Lett.* **2000**, *85*, 1930.
[17] A. Amirfazli, A. W. Neumann, *Adv. Colloid Interface Sci.* **2004**, *110*, 121.
[18] D. Quéré, *Nat. Mater.* **2004**, *3*, 79.
[19] T. Becker, F. Mugele, T. Pompe, S. Herminghaus, in *Thin Films: Preparation, Characterization, Applications*, (Eds: M. P. Soriaga, J. Stickney, L. W. Bottomley, Y.-G. Kim), Kluwer Academic/Plenum Publishers, New York **2002**, pp. 337–348.
[20] J. O. Indekeu, *Phys. A* **1992**, *183*, 439.
[21] R. G. Picknett, R. Bexon, *J. Colloid Interface Sci.* **1977**, *61*, 336.
[22] H.-Z. Yu, D. M. Soolaman, A. W. Rowe, J. T. Banks, *ChemPhysChem* **2004**, *5*, 1035.
[23] D. M. Soolaman, H.-Z. Yu, *J. Phys. Chem. B* **2005**, *109*, 17967.
[24] O. Wilhelm, PhD thesis, University of Tübingen (Germany) 2004.
[25] a) R. Wang, M. Kido, in *Science, Technology and Education of Microscopy: an Overview*, (Ed.: A. Méndez-Vilas), Formatex, Badajoz, Spain **2003**, pp. 10–16.
[26] R. G. Wang, M. Kido, *Mater. Lett.* **2003**, *57*, 2360.
[27] R. Wang, M. Kido, *Surf. Interface Anal.* **2005**, *37*, 1105.
[28] R. Wang, L. Cong, M. Kido, *Appl. Surf. Sci.* **2002**, *191*, 74.
[29] R. Wang, M. Takeda, M. Kido, *Mater. Lett.* **2002**, *54*, 140.
[30] R. Wang, M. Takeda, M. Kido, *Scr. Mater.* **2002**, *46*, 83.
[31] T. Pompe, A. Fery, S. Herminghaus, *Langmuir* **1998**, *14*, 2585.
[32] F. Mugele, T. Becker, R. Nikopoulos, M. Kohonen, S. Herminghaus, *J. Adhes. Sci. Technol.* **2002**, *16*, 951.
[33] O. V. Salata, *Curr. Nanosci.* **2005**, *1*, 25.
[34] S. N. Jayasinghe, M. J. Edirisinghe, *J. Aerosol. Sci.* **2002**, *33*, 1379.
[35] B. K. Ku, S. S. Kim, *J. Aerosol. Sci.* **2002**, *33*, 1361.
[36] B. K. Ku, S. S. Kim, Y. D. Kim, S. Y. Lee, *J. Aerosol. Sci.* **2001**, *32*, 1459.
[37] A. A. Naqwi, *J. Aerosol Sci.* **1994**, *25*, 1201.
[38] D. R. Chen, D. Y. H. Pui, S. L. Kaufman, *J. Aerosol. Sci.* **1995**, *26*, 963.
[39] B. G. Sumpter, D. W. Noid, M. D. Barnes, *Polymer* **2003**, *44*, 4389.
[40] M. D. Paine, M. S. Alexander, K. L. Smith, M. Wang, J. P. W. Stark, *J. Aerosol. Sci.* **2007**, *38*, 315.
[41] S. Adhikari, S. Fernando, *2006 ASAE Annual Meeting* **2006**, Paper number 066073.
[42] T. G. Mason, J. N. Wilking, K. Meleson, C. B. Chang, S. M. Graves, *J. Phys.: Condens. Matter* **2006**, *18*, R635.
[43] J. Koetz, S. Kosmella, *Polyelectrolytes and Nanoparticles*, Springer, Berlin **2007**.
[44] X. H. Zhang, W. Ducker, *Langmuir* **2008**, *24*, 110.
[45] X. H. Zhang, W. Ducker, *Langmuir* **2007**, *23*, 12478.
[46] A. P. Gunning, A. R. Mackie, P. J. Wilde, V. J. Morris, *Langmuir* **2004**, *20*, 116.
[47] A. Méndez-Vilas, M. L. González-Martín, M. J. Nuevo, *Ultramicroscopy* **2002**, *92*, 243.
[48] O. Tongcher, R. Sigel, K. Landfester, *Langmuir* **2006**, *22*, 4504.
[49] D. J. Stokes, B. L. Thiel, A. M. Donald, *Langmuir* **1998**, *14*, 4402.
[50] D. J. Stokes, *Adv. Eng. Mater.* **2001**, *3*, 126.
[51] R. G. Mathews, A. M. Donald, *Scanning* **2002**, *24*, 75.
[52] A. Checco, H. Schollmeyer, J. Daillant, P. Guenoun, R. Boukherroub, *Langmuir* **2006**, *22*, 116.
[53] D. Aronov, G. Rosenman, Z. Barkay, *J. Appl. Phys.* **2007**, *101*, 084901.
[54] A. Lafuma, D. Quéré, *Nat. Mater.* **2003**, *2*, 457.
[55] R. D. Narhe, D. A. Beysens, *Europhys. Lett.* **2006**, *75*, 98.
[56] A. Meister, M. Liley, J. Brugger, R. Pugin, H. Heinzelmann, *Appl. Phys. Lett.* **2004**, *85*, 6260.
[57] Y. C. Jung, B. Bhushan, *J. Vac. Sci. Technol. A* **2008**, *26*, 777.
[58] A. Fang, E. Dujardin, T. Ondarçuhu, *Nano Lett.* **2006**, *6*, 2368.
[59] K. T. Rodolfa, A. Bruckbauer, D. Zhou, A. I. Schevchuk, Y. E. Korchev, D. Klenerman, *Nano Lett.* **2006**, *6*, 252.
[60] D. Saya, T. Leïchle, J. B. Pourciel, C. Bergaud, L. Nicu, *J. Micromech. Microeng.* **2007**, *17*, N1.
[61] H. D. Espinosa, K.-H. Kim, N. Moldovan, in *Nanodevices for the Life Sciences*, (Ed.: C. S. S. R. Kumar), Wiley-VCH, Weinheim, Germany **2006**, pp. 109–149.

[62] T. Ondarçuhu, L. Nicu, S. Cholet, C. Bergaud, S. Gerdes, C. Joachim, *Rev. Sci. Instrum.* **2000**, *71*, 2087.
[63] M. B. Ali, T. Ondarçuhu, M. Brust, C. Joachim, *Langmuir* **2002**, *18*, 872.
[64] C. Gupta, G. A. Mensing, M. A. Shannon, P. J. Kenis, *Langmuir* **2007**, *23*, 2906.
[65] S. Uemura, M. Stjernström, J. Sjödahl, J. Roeraade, *Langmuir* **2006**, *22*, 10272.
[66] Y. Martin, C. C. Williams, H. K. Wickramasinghe, *J. Appl. Phys.* **1987**, *61*, 4723.
[67] Q. Zhong, D. Inniss, K. Kjoller, V. B. Elings, *Surf. Sci.* **1993**, *290*, L688.
[68] R. García, R. Magerle, R. Pérez, *Nat. Mater.* **2007**, *6*, 405.
[69] B. Reutter, A. Checco, Y. Cai, O. Gang, B. M. Ocko, "Using Non-Contact AFM to Image Liquid Topographies", **2007**, http://cp.literature.agilent.com/litweb/pdf/5989-6515 EN.pdf (accessed February 2009).
[70] A. Checco, Y. Cai, O. Gang, B. M. Ocko, *Ultramicroscopy* **2006**, *106*, 703.
[71] S. Herminghaus, A. Fery, D. Reim, *Ultramicroscopy* **1997**, *69*, 211.
[72] S. Haferl, D. Poulikakos, Z. Zhao, *Exp. Heat Transfer* **2001**, *14*, 1.
[73] J. Tamayo, R. García, *Langmuir* **1996**, *12*, 4430.
[74] R. Szoszkiewicz, E. Riedo, *Phys. Rev. Lett.* **2005**, *95*, 135502.
[75] E. Riedo, F. Lévy, H. Brune, *Phys. Rev. Lett.* **2002**, *88*, 185505.
[76] H. Schönherr, G. J. Vancso, in *Scanning Probe Microscopies Beyond Imaging: Manipulation of Molecules and Nanostructures*, (Ed.: P. Samori), Wiley-VCH, Weinheim, Germany **2006**, pp. 275–314.
[77] A. Noy, D. V. Vezenov, C. M. Lieber, in *Handbook of Molecular Force Spectroscopy*, (Ed.: A. Noy), Springer, Berlin **2008**, pp. 97–122.
[78] Z. Wei, C. Wang, Z. Wang, D. Liu, C. Bai, *Surf. Interface Anal.* **2001**, *32*, 275.
[79] Z. Liu, Z. Li, H. Zhou, G. Wei, Y. Song, L. Wang, *Micron* **2005**, *36*, 525.
[80] A. Méndez-Vilas, A. B. Jódar-Reyes, J. Díaz, M. L. González-Martín, *Curr. Appl. Phys.* **2009**, *9*, 48.
[81] M. Schenk, M. Füting, R. Reichelt, *J. Appl. Phys.* **1998**, *84*, 4880.
[82] K. Fei, C. P. Chiu, C. W. Hong, *Microfluid. Nanofluid.* **2008**, *4*, 321.
[83] T. E. Schäffer, in *Force Microscopy: Applications in Biology and Medicine*, (Eds: B. P. Jena, J. K. H. Hörber), John Wiley & Sons, Hoboken, NJ **2006**, pp. 221–248.
[84] P. K. Hansma, G. Schitter, G. E. Fantner, C. Prater, *Science* **2006**, *314*, 601.
[85] G. E. Fantner, P. Hegarty, J. H. Kindt, G. Schitter, G. A. G. Cidade, P. K. Hansma, *Rev. Sci. Instrum.* **2005**, *76*, 026118.
[86] M. J. Rost, L. Crama, P. Schakel, E. van Tol, G. B. E. M. van Velzen-Williams, C. F. Overgauw, H. ter Horst, H. Dekker, B. Okhuijsen, M. Seynen, A. Vijftigschild, P. Han, A. J. Katan, K. Schoots, R. Schumm, W. van Loo, T. H. Oosterkamp, J. W. M. Frenken, *Rev. Sci. Instrum.* **2005**, *76*, 053710.
[87] A. G. Onaran, M. Balantekin, W. Lee, W. L. Hughes, B. A. Buchine, R. O. Guldiken, Z. Parlak, C. F. Quate, F. L. Degertekin, *Rev. Sci. Instrum.* **2006**, *77*, 023501.
[88] N. V. Churaev, V. M. Starov, B. V. Derjaguin, *J. Colloid Interface Sci.* **1982**, *89*, 16.
[89] L. Yang, I. Akhatov, M. Mahinfalah, B. Z. Jang, *J. Chin. Inst. Eng.* **2007**, *30*, 441.
[90] A. K. H. Cheng, D. M. Soolaman, H.-Z. Yu, *J. Phys. Chem. B* **2007**, *111*, 7561.
[91] G. D. Danilatos, *Microsc. Res. Tech.* **1993**, *25*, 354.
[92] A. M. Donald, *Nat. Mater.* **2003**, *2*, 511.
[93] M. Toth, M. R. Phillips, *Scanning* **2000**, *22*, 370.
[94] Q. F. Wei, R. R. Mather, A. F. Fotheringham, R. D. Yang, *Text. Res. J.* **2003**, *73*, 557.
[95] N. A. Stelmashenko, J. P. Craven, A. M. Donald, E. M. Terentjev, B. L. Thiel, *J. Microsc.* **2001**, *204*, 172.
[96] M. Brugnara, C. Della Volpe, S. Siboni, D. Zeni, *Scanning* **2006**, *28*, 267.
[97] S. Kitching, A. M. Donald, *J. Microsc.* **1998**, *190*, 357.
[98] C. P. Royall, B. L. Thiel, A. M. Donald, *J. Microsc.* **2001**, *204*, 185.
[99] D. J. Stokes, *Infocus Mag. Proc. R. Microsc. Soc.* **2006**, *2*, 64.
[100] R. E. Cameron, A. M. Donald, *J. Microsc.* **1994**, *173*, 227–237.
[101] M. Toth, F. S. Baker, *Microsc. Microanal.* **2004**, *10*, 1062.
[102] M. Toth, W. R. Knowles, B. L. Thiel, *Appl. Phys. Lett.* **2006**, *88*, 023105.
[103] Y. Gu, *Colloids Surf. A* **2001**, *181*, 215.
[104] A. Kiraz, Y. Karadağ, A. F. Coskun, *Appl. Phys. Lett.* **2008**, *92*, 191104.
[105] M. Sundberg, A. Månsson, S. Tågerud, *J. Colloid Interface Sci.* **2007**, *313*, 454.
[106] S. N. Gorb, D. Voigt, E. V. Gorb, in *Modern Research and Educational Topics in Microscopy*, (Eds: A. Méndez-Vilas, J. Díaz), Formatex, Badajoz, Spain **2007**, pp. 812–819.
[107] A. Checco, P. Guenoun, J. Daillant, *Phys. Rev. Lett.* **2003**, *91*, 186101.
[108] V. Dupres, T. Camesano, D. Langevin, A. Checco, P. Guenoun, *J. Colloid Interface Sci.* **2004**, *269*, 329.
[109] V. Dupres, D. Langevin, P. Guenoun, A. Checco, G. Luengo, F. Leroy, *J. Colloid Interface Sci.* **2007**, *306*, 34.
[110] A. Moosavi, M. Rauscher, S. Dietrich, *Langmuir* **2008**, *24*, 734.
[111] A. B. Jódar-Reyes, A. Méndez-Vilas, M. L. González-Martín, in *Modern Research and Educational Topics in Microscopy*, (Eds: A. Méndez-Vilas, J. Díaz), Formatex, Badajoz, Spain **2007**, pp. 500–512.
[112] J. Fraxedas, A. Verdaguer, F. Sanz, S. Baudron, P. Batail, *Surf. Sci.* **2005**, *588*, 41.
[113] N. Missert, R. G. Copeland, *Appl. Surf. Sci.* **2008**, *254*, 1972.
[114] T. E. Karis, U. Nayak, *Tribol. Trans.* **2004**, *47*, 103.
[115] T. E. Karis, M. A. Tawakkul, *Tribol. Trans.* **2003**, *46*, 469.
[116] S. D. A. Connell, S. Allen, C. J. Roberts, J. Davies, M. C. Davies, S. J. B. Tendler, P. M. Williams, *Langmuir* **2002**, *18*, 1719.
[117] A. Méndez-Vilas, M. G. Donoso, J. L. González-Carrasco, M. L. González-Martín, *Colloids Surf. B* **2006**, *52*, 157.
[118] A. Méndez-Vilas, J. M. Bruque, M. L. González-Martín, *Ultramicroscopy* **2007**, *107*, 617.
[119] R. Hofer, M. Textor, N. D. Spencer, *Langmuir* **2001**, *17*, 4123.
[120] K. K. S. Lau, J. Bico, K. B. K. Teo, M. Chhowalla, G. A. J. Amaratunga, W. I. Milne, G. H. McKinley, K. K. Gleason, *Nano Lett.* **2003**, *3*, 1701.
[121] Y. T. Cheng, D. E. Rodak, *Appl. Phys. Lett.* **2005**, *86*, 144101.
[122] Y. C. Jung, B. Bhushan, *J. Microsc.* **2008**, *229*, 127.
[123] K. Van de Velde, P. Kiekens, *Indian J. Fibre Text. Res.* **2000**, *25*, 8.
[124] Q. F. Wei, X. Q. Wang, R. R. Mather, A. F. Fotheringham, *Fibres Text. East. Eur.* **2004**, *12–2*, *79*.
[125] H. Sawada, S. Shioya, Y. Takasaki, K. Namba, H. Yamabayashi, *Tohoku J. Exp. Med.* **1978**, *124*, 233.
[126] B. J. Carroll, *J. Colloid Interface Sci.* **1976**, *57*, 488.
[127] Q. F. Wei, R. R. Mather, A. F. Fotheringham, R. D. Yang, *J. Aerosol Sci.* **2002**, *33*, 1589.
[128] Q. F. Wei, R. R. Mather, A. F. Fotheringham, R. D. Yang, J. Buckman, *Oil Gas Sci. Technol.* **2003**, *58*, 593.
[129] Q. F. Wei, *Mater. Charact.* **2004**, *52*, 231.
[130] O. Carmody, R. Frost, Y. Xi, S. Kokot, *Surf. Sci.* **2007**, *601*, 2066.
[131] J. O. Buckman, "Wettability Studies of Petroleum Reservoir Rocks", *ESEM Application Note, FEI/Phillips* **2008**, http://www.pet.hw.ac.uk/cesem/pdfbin/feinote.pdf (accessed February 2009).
[132] T. M. Okasha, J. J. Funk, H. N. Al-Rashidi, *J. Pet. Technol.* **2008**, *Jan*, 53.
[133] H. M. Yu, J. O. Schumacher, M. Zobel, C. Hebling, *J. Power Sources* **2005**, *145*, 216.
[134] H. M. Yu, C. Ziegler, M. Oszcipok, M. Zobel, C. Hebling, *Electrochim. Acta* **2006**, *51*, 1199.

[135] A. Liukkonen, *Scanning* **1997**, *19*, 411.
[136] L. Valentini, F. Mengoni, J. M. Kenny, A. Marrocchi, A. Taticchi, *Small* **2007**, *3*, 1200.
[137] C. Joachim, J. K. Gimzewski, A. Aviram, *Nature* **2000**, *408*, 541.
[138] D. Aronov, M. Molotskii, G. Rosenman, *Appl. Phys. Lett.* **2007**, *90*, 104104.
[139] D. Aronov, M. Molotskii, G. Rosenman, *Phys. Rev. B* **2007**, *76*, 035437.
[140] M. Morita, T. Koga, H. Otsuka, A. Takahara, *Langmuir* **2005**, *21*, 911.
[141] M. Morita, "Photolithographic method of producing complex shapes of monolayer films. Anisotropic wetting on the patterned organic monolayer surface." **2008**, http://www.nanonet. go.jp/japanese/facility/report/m-004.pdf (accessed February 2009).
[142] J. Léopoldès, P. Damman, *Nat. Mater.* **2006**, *5*, 957.
[143] A. Checco, O. Gang, B. M. Ocko, *Phys. Rev. Lett.* **2006**, *96*, 056104.
[144] K. Khare, S. Herminghaus, J.-C. Baret, B. M. Law, M. Brinkmann, R. Seemann, *Langmuir* **2007**, *23*, 12997.
[145] K. Fukuzawa, T. Deguchi, J. Kawamura, Y. Mitsuya, T. Muramatsu, H. Zhang, *Appl. Phys. Lett.* **2005**, *87*, 203108.
[146] R. Seemann, M. Brinkmann, E. J. Kramer, F. F. Lange, R. Lipowsky, *Proc. Natl. Acad. Sci. USA* **2005**, *102*, 1848.
[147] F. Dubreuil, J. Daillant, P. Guenoun, *Langmuir* **2003**, *19*, 8409.

Received: June 10, 2008
Revised: March 3, 2009